JOURNAL OF GEOPHYSICAL RESEARCH, VOL. 103, NO. C6, PAGES 12,689–12,708, JUNE 15, 1998

Subtidal energetics in the Faroe-Shetland Channel: Coarse-grid model experiments

L.-Y. Oey

Atmospheric and Oceanic Sciences Program, Princeton University, Princeton, New Jersey

Abstract. This paper compares various forcings that contribute to the regional subtidal energetics of the ocean passageway northwest of Scotland, in the Faroe-Shetland Channel (FSC), where inflow of warm and saline North Atlantic water mixes with outflow of cold and less-saline Nordic Sea waters. On the scales resolvable by the (coarse) grid sizes of $\Delta x = \Delta y = 20$ km and 20 vertical sigma layers, changes in currents' energetics caused by wind, Atlantic inflow (doubled), decreased horizontal mixing, surface heat flux, and open-boundary density specifications were 28, 43, 40, 16, and 5%, respectively, of the kinetic energy of a background quasi-steady slope current. The subtidal currents were not sensitive to the atmospheric pressure forcing and the surface relaxation to monthly climatology nor to the inclusion of additional (apart from M2) tidal constituents K1, O1, and S2. Wind-induced motions resulted in transport fluctuations of about 1.5 Sv in the FSC, maximum in winter and minimum in summer, and alongshore and cross-shore current variances of 0.1 and 0.05 m s^{-1}, respectively, in fair agreement with observations. Spectral peaks at periods of 23–30 hours were found and were shown to correspond to resonant continental shelf waves in the channel.

1. Introduction

The ocean passageway between the north/northwestern Scottish-Irish coast/Shetland Island and the Faroe Islands/Rockall Bank (Figure 1) (hereinafter referred to as the northwest approaches (NWA)), including the Faroe-Shetland Channel (FSC) and the Rockall Channel, represents an important conduit through which the warm and saline North Atlantic water (potential temperature $T > 8°C$ and salinity $S > 35$ practical salinity units (psu)) flows into the ocean regions farther to the north (the Norwegian Sea and North Sea, in particular). Estimates of the near-surface inflow range from 2 Sv (1 Sv = 10^6 m^3 s^{-1}) by *Dooley and Meincke* [1981] to 9 Sv by *Worthington* [1970], but more recent data based on direct current-meter measurements suggest a value of around 5 Sv [*Saunders*, 1990], with possibly large fluctuations of about 1–2 Sv. The Faroe-Shetland Channel, together with the Faroe Bank Channel and a narrow (<10 km wide) notch in the Wyville-Thomson Ridge, is also an escape route for about 20–30% (~1–2 Sv [*Hopkins*, 1991; *Saunders*, 1990]) of the outflow of cold and less-saline Nordic Sea waters into the Atlantic, again with possibly large fluctuations (about 0.5 Sv). The ability to accurately model the spatial distributions of these transports and their temporal variability is clearly important to a fuller understanding of the Arctic/Atlantic connection, hence also to the climate system. The present work is more limited, however, and focuses on characterizing currents in relation to engineering requirements of offshore oil and gas exploration in the FSC. The ultimate goal is to account for both large-scale (e.g., wind-induced) as well as mesoscale (e.g., frontal meanders and eddies) components of the circulation by coupling a limited-area model to a large-scale ocean circulation model, for example. This paper focuses on assessing the relative importance of the various forcings that contribute to the large-scale subtidal energetics, as well as the sensitivity of the currents to model parameters. A follow-up work [*Oey*, 1998] examines the mesoscale meanders and eddies. Section 2 reviews the forcing and regional circulation. Section 3 describes the model. Sections 4 and 5 discuss the model results and the sensitivity experiments and relate these to observations whenever possible. The paper ends with a concluding summary in section 6.

Paper number 98JC00786.
0148-0227/98/98JC-00786$09.00

2. NWA Regional Physical Oceanography: A Brief Review

One prominent feature of the large-scale circulation in the NWA is the existence of a northward flowing slope current associated with a core of warm water normally observed over

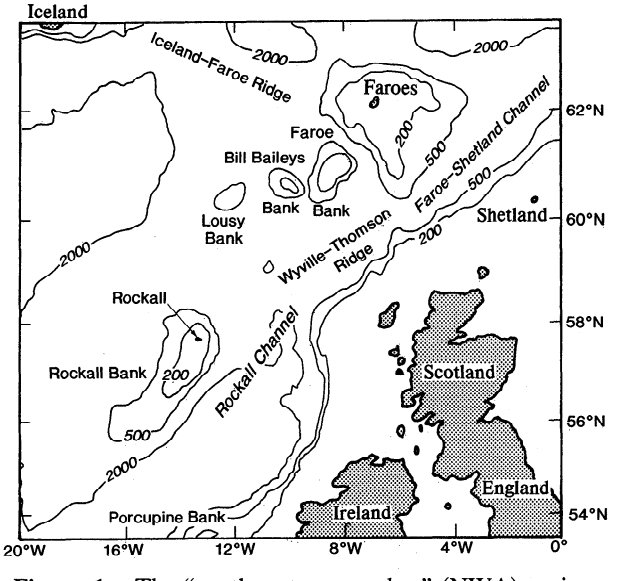

Figure 1. The "northwest approaches" (NWA) region.

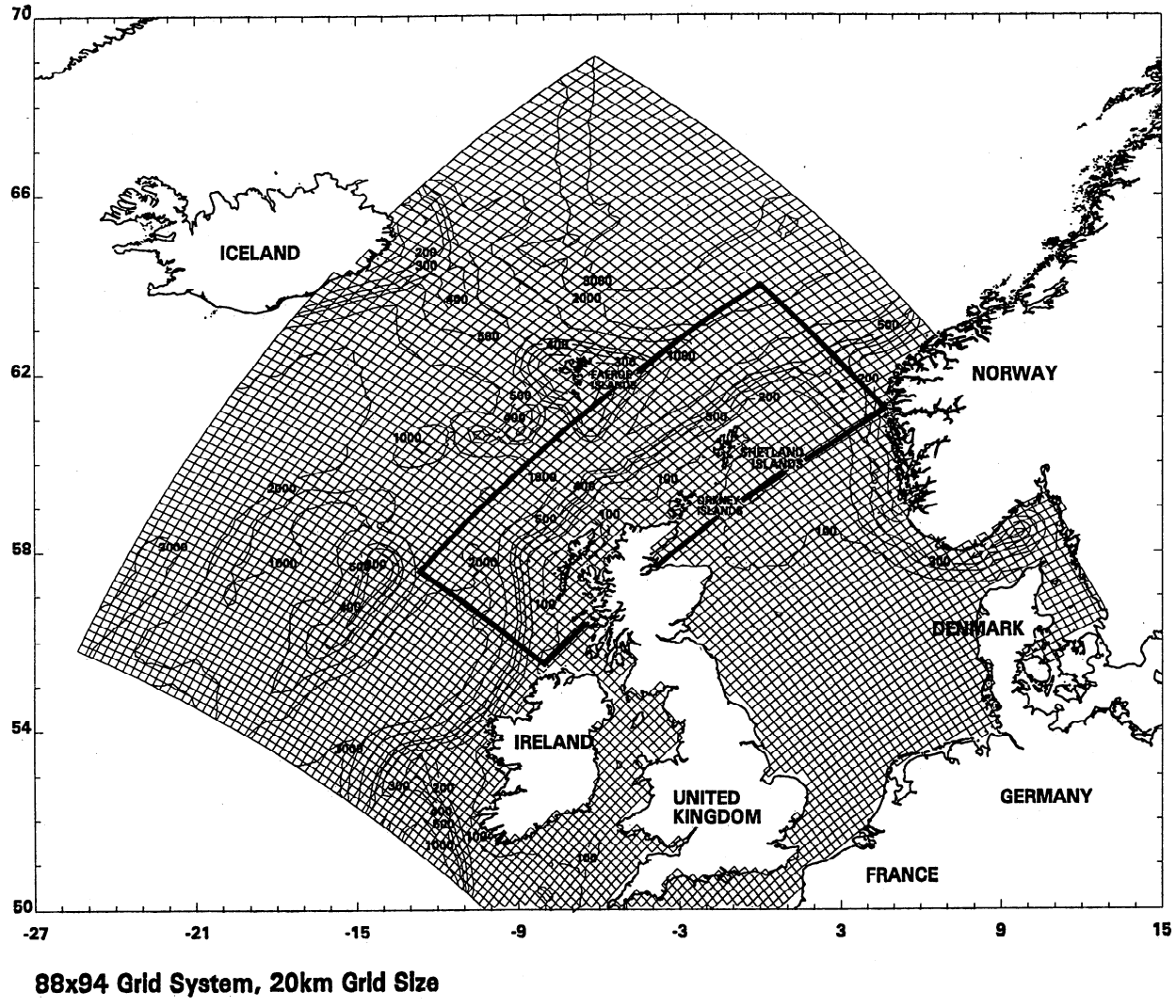

Figure 2a. Topography (in meters) of the model region. The NWA subregion where model results are analyzed in detail is enclosed in a rectangle.

the shallow side of the slope [*Booth and Ellett*, 1983]. The total transport is over 1 Sv, and current speeds (near 57°N, 9.5°W and water depth of 992 m) are about 0.1–0.2 m s^{-1}. These currents are generally more intense farther north over the Scottish slope and in the Faroe-Shetland Channel [*Ellett et al.*, 1986; *Saunders*, 1990], where flow speeds in excess of 1 m s^{-1} had been reported [*Hopkins*, 1991], and are weaker to the south off the Porcupine Bank (52°N, 15°W [*Huthnance*, 1984]). Currents in the south exhibited weak shear down to a depth of about 500 m [see *Booth and Ellett*, 1983, Figure 2], and means were 0.16 m s^{-1} at 90 m and 0.09 m s^{-1} at 490 m. The driving force appears to be an along-slope pressure gradient, with a corresponding surface slope of 1 cm/100 km [*Huthnance*, 1984].

Superimposed on the slope current are shorter-time variabilities due to tides [*Cartwright et al.*, 1980], meanders and eddies [*Dooley et al.*, 1976; *Booth*, 1988], and winds [*Dickson et al.*, 1986; *Meincke*, 1986; *Huthnance*, 1986; *Gordon and Huthnance*, 1987]. Tidal currents are weak in the Rockall Channel and shelf (≈0.1 m s^{-1}) and are more significant off the northern Scottish coast/Shetland Island (≈0.3 m s^{-1} [e.g., *Xing and Davies*, 1996a; *Davies et al.*, 1997]). Perhaps of more importance is the generation and propagation of internal tides near the shelf break, which produce intense currents near the seabed (≈0.2 m s^{-1}), intense vertical shears (≈2×10^{-3} s^{-1}), and large isopycnal displacements (≈30 m [*Xing and Davies*, 1996b]). Internal tides would require high resolution ($\Delta < 5$ km and 20 or more layers [*Cummins and Oey*, 1997]) and are not resolved by the coarse grids used in the present work.

While eddy-induced variability has generally been observed off the slope in deeper waters [*Booth and Ellett*, 1983], satellite images and in situ measurements also indicate current meanders along the slope. In the FSC, *Dooley et al.* [1976] gave evidence of northeastward meander (eddy?) propagation, with current speeds of about 0.4–0.55 m s^{-1} at 100 m (over a water depth of 1000 m near 60.5°N, 5.5°W). Eddies are also found in the deeper Rockall Channel [*Booth*, 1988], with peak orbital speeds >0.8 m s^{-1} near the surface. Little is known about the nature and cause of these meanders and eddies, though flow instability has been suggested [*Huthnance*, 1986; *Booth*, 1988].

In the wind-induced subtidal timescales, observations [*Huthnance*, [1983] suggest motions due to coastally trapped waves (CTW). *Huthnance* [1986] and *Gordon and Huthnance* [1987] show that over the Scottish continental shelf (currents at 61.5°N, 0°E, 159-m water depth and 60°N, 4°W, 122-m water depth), two types of response to winter storms (wind stress about 1 Pa or more) exist: high-frequency (about 0.6f, where f is the Coriolis

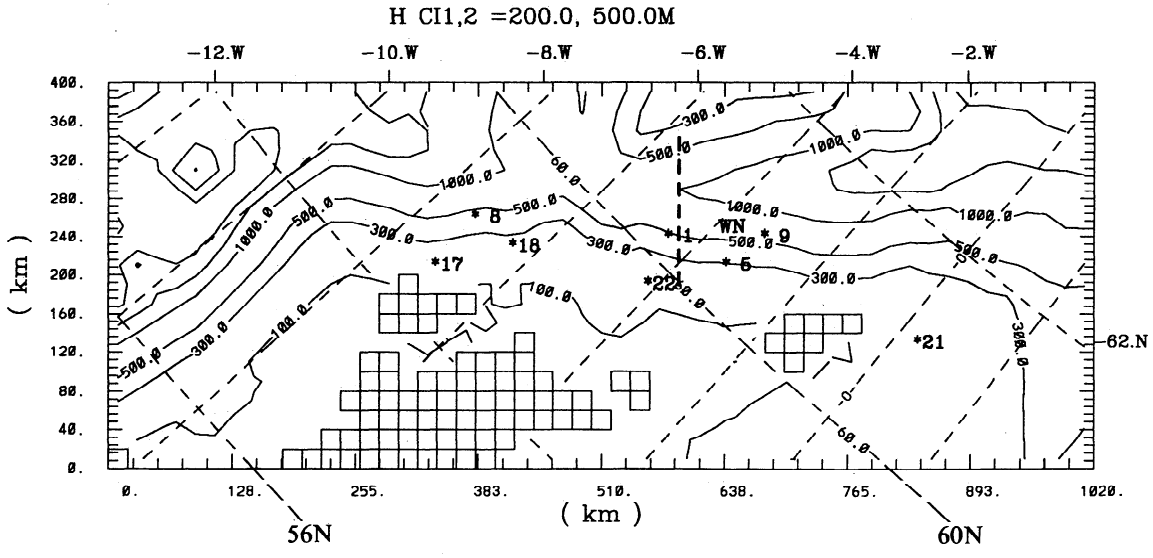

Figure 2b. The NWA subregion with locations of current meter (asterisks) and wind (WN) stations: 1-BP204/24, 8-BP164/25, 17-HN83-STN2, 22-Fitzroy, 18-HN83-STN3, 5-SH205/14, 9-SH206/01, and 21-Stevenson. The Faroe-Shetland section, discussed in text, is indicated as a thick dashed line.

parameter) clockwise-rotating currents caused by localized forcing of short duration and quasi-steady currents caused by more extensive along-shelf forcing, in which along-isobath current amplitude increased as long as the wind blew and stopped when the wind stopped. Responses were barotropic with amplitudes of about 0.2–0.4 m s^{-1}. The first response was near the maximum frequency of the first CTW mode dispersion curve, where the group velocity is zero, and the second was near the low-frequency, linear portion of the curve, where the group velocity is positive (propagation with the coast on the right in the northern hemisphere). These responses have been predicted by idealized models [*Heaps et al.*, 1988].

This work focuses on modeling the slope current and wind-induced response in the NWA region off the Scottish slope and shelf (the FSC in particular) and on identifying model forcing and parameters which are important. While the four dominant tidal constituents, M2, S2, K1, and O1, are included in the calculations, they are used only to provide mixing and energy dissipation for the low-frequency motions.

3. Model

To account for some of the large-scale dynamics that can impact the circulation in the NWA region, a model domain that extends from 47° to 68°N, and 25°W to 15°E was chosen (Figure 2). The model y axis is tilted 45° clockwise from true north so that the x component velocity is approximately along slope in the NWA region.

3.1. Governing Equations

The model [*Oey and Chen*, 1992] (hereinafter referred to as OC) solves the finite-difference analog of the following set of equations assuming that the ocean is incompressible and hydrostatic and using the Boussinesq approximation

$$\nabla \cdot \mathbf{u} + \partial w/\partial z = 0 \tag{1a}$$

$$\partial \mathbf{u}/\partial t + \mathbf{u} \cdot \nabla \mathbf{u} + w\partial \mathbf{u}/\partial z + f\mathbf{k}\mathbf{X}\mathbf{u} = -\nabla p/\rho_0 + \partial(K_M \partial \mathbf{u}/\partial z)/\partial z + \mathbf{F}_M \tag{1b}$$

$$\rho g = -\partial p/\partial z \tag{1c}$$

$$\partial e/\partial t + \mathbf{u} \cdot \nabla e + w\partial e/\partial z = \partial(K_H \partial e/\partial z)/\partial z + F_H \tag{1d}$$

$$\rho = \rho(T, S, p) \tag{1e}$$

Here ∇ is the horizontal gradient operator, $\mathbf{u} = (u, v)$ is the horizontal velocity vector, and w is the vertical component of velocity; e denotes either the temperature T or the salinity S, which are related to density ρ through an equation of state (1e) [*Mellor*, 1991]; $f = 2\Omega \sin(\phi)$, where $\Omega = 7.292 \times 10^{-5}$ s^{-1} and ϕ is the latitude. The $\mathbf{F}_M$ and F_H are Laplacian-type horizontal viscosity and diffusion terms, respectively, with coefficients A_M and A_H taken to be equal, modeled by the Smagorinsky diffusion formulation (OC)

$$A_M = A_H = C\Delta x \Delta y[u_x^2 + v_y^2 + (u_y + v_x)^2/2]^{1/2} \tag{2}$$

where C is a constant which will be varied in the sensitivity experiments to be described below. Typical values of A_M and A_H are 20–200 m^2 s^{-1}, and these vary approximately linearly with "C" [cf. *Oey*, 1996a]. Vertical turbulent mixing is modeled through the use of the eddy viscosity and diffusivity, K_M and K_H, respectively, according to the level-2.5 turbulence closure scheme of *Mellor and Yamada* [1982]. Constant horizontal grid spacings $\Delta x = \Delta y = 20$ km and 20 equally spaced sigma layers in the vertical were used. The model has a free surface, and for computational efficiency, time integration is split into a two-dimensional, external mode with a short time step of 40 s and a three-dimensional internal mode with a long time step of 20 min. Bathymetry was from the U.S. Navy DBDB-5, interpolated onto the model grid. The pressure-gradient error in sigma coordinate was checked with a 60-day calculation with no forcing and with density a function of the vertical coordinate "z" only (i.e., level isopycnals [cf. *Oey*, 1996b]). This gave a maximum speed of $O(10^{-3}$ m $s^{-1})$ and transport of $O(0.03$ Sv), small in comparison to typical simulated values of $O(0.1$ m $s^{-1})$ and $O(1$ Sv).

3.2. Boundary Conditions

The normal velocities are zeros at all sidewalls. In the C-grid system, which the model employs, the tangential velocities are

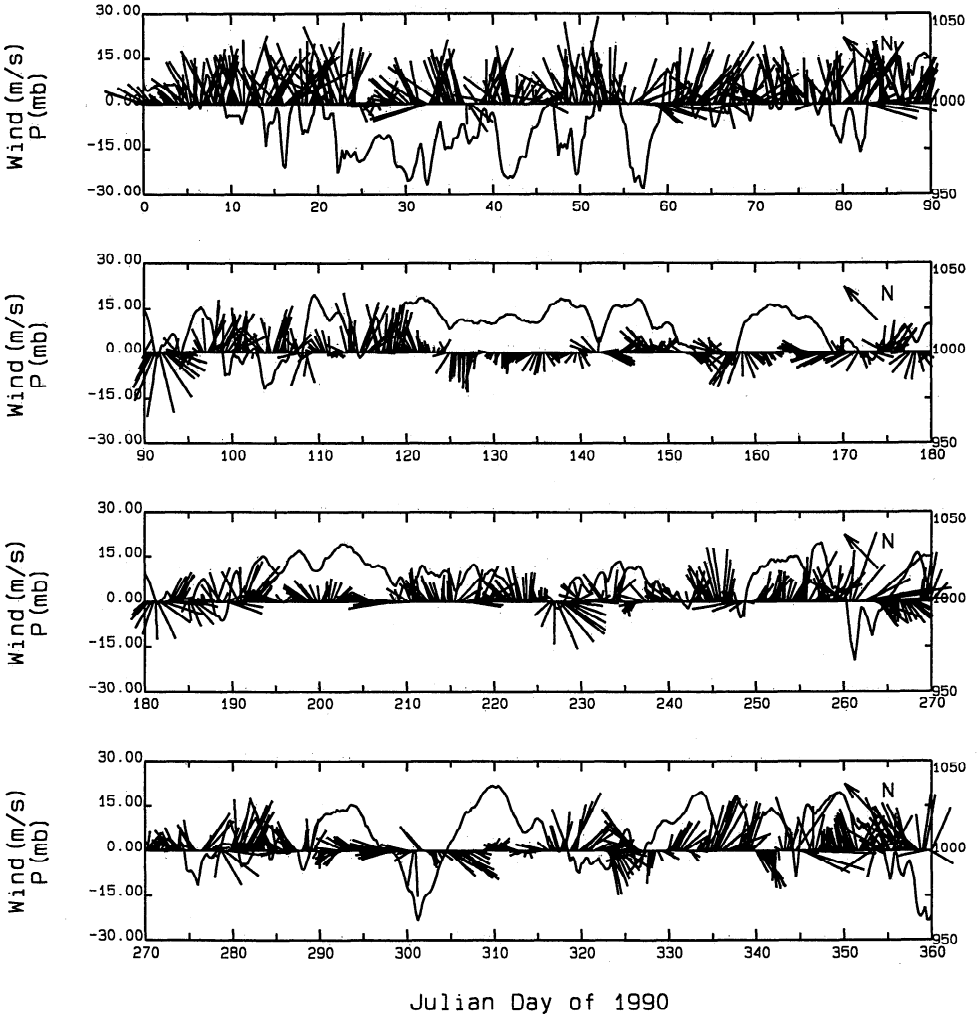

Figure 3. Wind and pressure at station WN (Figure 2b) for 1990. The vector sticks are rotated such that upward sticks in the figure point in the model's positive x direction (i.e., northeastward).

also set zeros at half-grid distance inside the walls. At the free surface, $z \rightarrow \eta(x, y, t)$

$$K_M(\partial u/\partial z, \partial v/\partial z) = (\tau_o^x, \tau_o^y) \quad (3a)$$

$$K_H(\partial T/\partial z, \partial S/\partial z) = (T_{os}, S_{os}) \quad (3b)$$

$$w = \partial \eta/\partial t + \mathbf{u} \cdot \nabla \eta \quad (3c)$$

Here τ_o is the (kinematic) wind stress vector and

$$T_{os} = -Q/(\rho_o C_{pw}) + C_1(T_{cs} - T) \quad (4a)$$

$$S_{os} = S_s(E - P)/\rho_o + C_1(S_{cs} - S) \quad (4b)$$

where Q is the total heat flux in W m^{-2}, positive upward; C_{pw} is the specific heat for water, taken from *Gill* [1982] to be 4000

Table 1. Sensitivity Experiments

Experiment Number	Wind*	Tides	Surface Relax, days	Surface Heat Flux	Horizontal Viscosity "C"	Atmospheric Pressure*	Boundary T and S	Atlantic Inflow, Sv
0	6 hourly	M2, S2, K1, O1	300	*Bunker* [1976]	0.20	6 hourly	monthly	5
1	0	...	...	...	...	0	...	...
2	...	M2	...	...	...	...	...	...
3	...	...	...	...	0.10	...	...	...
4	...	...	...	...	0.05	...	...	...
5	...	...	...	0	...	...	...	...
6	...	...	...	...	...	0	...	...
7	...	...	...	...	...	...	annual	...
8	...	...	...	...	...	...	...	10
9	...	...	30	...	...	...	...	...

Dots represent values that are the same as base experiment 0.
*From the Norwegian Meteorological Institute (DNMI).

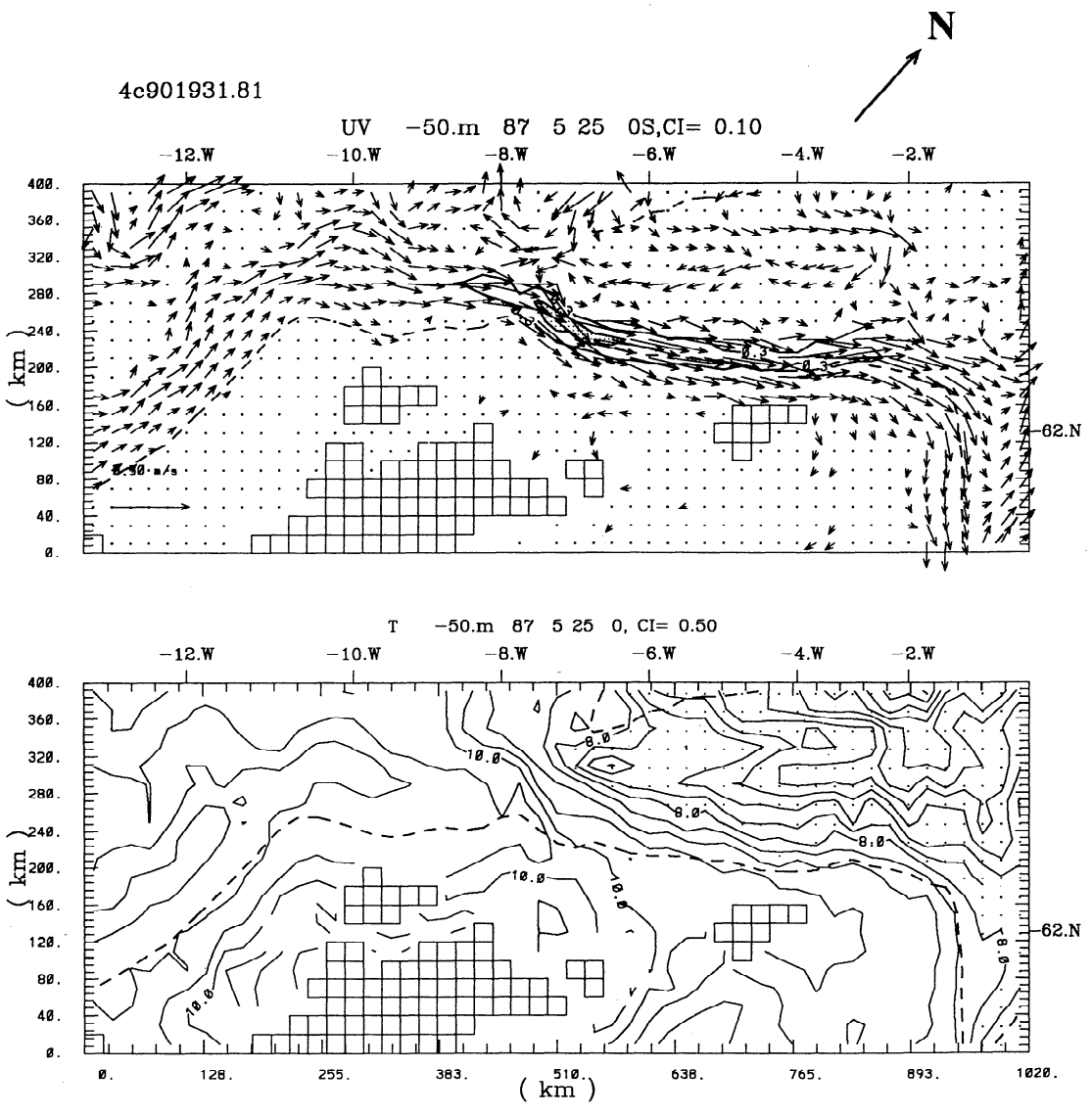

Figure 4. Model currents and temperature (contour interval (CI) = 0.5°C) at $z = -50$ m on May 25, 1987 (experiment 0). Solid contours on the vector plot show currents' speeds (CI = 0.1 m s^{-1}), stippled for values over 0.4 m s^{-1}. Stippled region in the temperature plot is where $T < 8$°C. Dashed contours show the 300-m isobath.

J kg^{-1} K^{-1}, $(E - P)$ is the net evaporation minus precipitation rate in kg m^{-2} s^{-1}; S_s is the surface salinity taken as being equal to the salinity at the first sigma level near the surface; T_{cs} and S_{cs} are climatological surface temperature and salinity, respectively, taken from *Levitus*' [1982] monthly values; and C_1 is a relaxation constant with a unit of m s^{-1}. For small $|Q|$ and $(E - P)$ and in the absence of fluxes due to other physical processes (e.g., advection or river discharge) the temperature and salinity in the upper h_1 meters (say) of the ocean adjusts to their respective climatological values on a timescale of h_1/C_1 seconds. The value of C_1 is chosen as 3.47×10^{-8} m s^{-1}, which gives a relaxation timescale of about 1 year at the surface. The heat flux "Q" has an annual-averaged spatial function, $B(x, y)$, modulated in time with an annual cycle, and approximates the values in W m^{-2} given by *Bunker* [1976]

$$Q = B(x, y) + 180 \sin[2\pi(t - t_o)/P] \quad (5)$$

where t_o is the Julian day that corresponds to September 10 of the year and P is the number of days in that year. This specification is clearly ad hoc, but the sensitivity test discussed below suggests that a more exact prescription would not significantly change the results. The function "$(E - P)$" is uncertain and is set to zero so that the surface salt flux is simply relaxed to the climatological values. Six-hour wind vectors, $\mathbf{U}_w$, (and atmospheric pressure) were obtained from the atmospheric boundary layer model of the Norwegian Meteorological Institute. As an example, the wind vector and pressure at $(x, y) = (1200, 1160)$ km (station "WN" in Figure 2b) for 1990 are shown in Figure 3. Analyses of the 11-year wind maps (from 1985 to 1995, not shown) indicate that the monthly mean wind is generally from the southwest and most intense during the winter months when the region is dominated by passages of cyclones as indicated, for example, by large-amplitude bursts of low pressures in Figure 3, and weakest in April through June. The winds are converted to stresses in m^2 s^{-2} using *Smith*'s [1980] formula

$$\tau_o = C_d|\mathbf{U}_w|\mathbf{U}_w \quad (6)$$

where $C_d = 10^{-6}$ for $|\mathbf{U}_w| < 6$ m s^{-1} and $C_d = (0.61 + 0.063\ |\mathbf{U}_w|) \times 10^{-6}$ otherwise. As in OC, the atmospheric pressure is added to the pressure term in (1b).

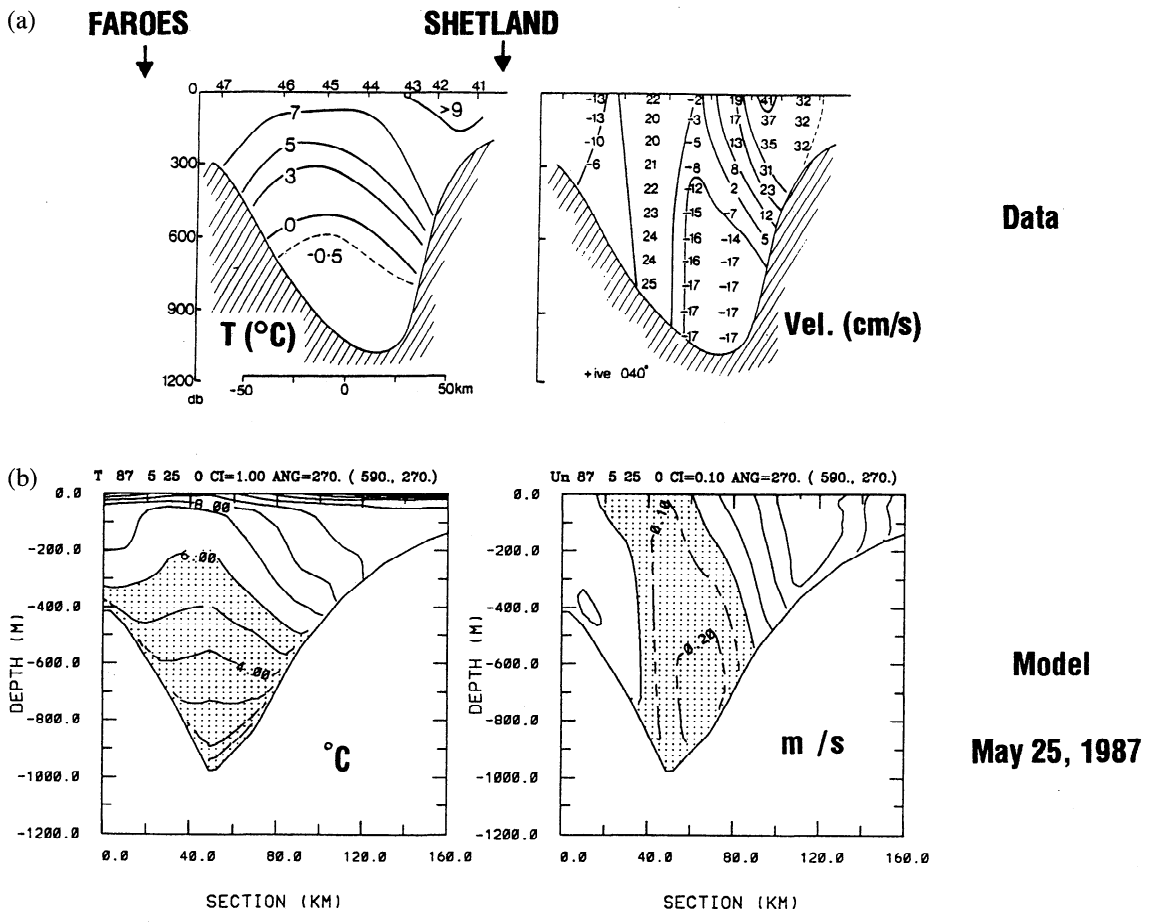

Figure 5. (a) Observed [from *Saunders*, 1990] and (b) modeled temperature and normal velocity contours across the Faroe-Shetland Channel section (Figure 2b; view is looking northeastward, so that the right side of Figures 5a and 5b is the Scottish shelf, i.e., "Shetland" side).

At the ocean floor, $z = -H(x, y)$, salt and heat fluxes are zero while momentum flux is balanced by matching the computed velocity, $\mathbf{u}_b$, nearest the bottom, $z = z_b$, with the logarithmic law of the wall

$$K_M(\partial \mathbf{u}/\partial z) = C_D|\mathbf{u}_b|\mathbf{u}_b \tag{7a}$$

where $C_D = \max\{2.5 \times 10^{-3}, (k/\ln[(H + z_b)/z_r])^2\}$, $k = 0.40$ is the von Karman's constant, H is local depth, and z_r (~ 0.005 m) is the roughness height. C_D increases from about 10^{-2} in shallow waters where $H \sim 5$ m to about 2.7×10^{-3} in shelf break regions where $H \sim 200$ m; in deeper waters ($H > 300$ m) where the logarithmic layer cannot be resolved, $C_D = 2.5 \times 10^{-3}$. Finally, the requirement that the ocean bottom is a material surface gives

$$w = -\mathbf{u} \cdot \nabla H \tag{7b}$$

Details of the open boundary conditions are described in OC, and only a brief outline is given here. Inflow of 5 Sv (1 Sv = 10^6 m^3 s^{-1}) is linearly distributed along the "western" boundary (i.e., the boundary stream function is zero west of Ireland at 15°W, 52.5°N and increases linearly along the boundary to 5 Sv just south of Iceland), and this together with the Baltic discharge (with $S = 0$) is allowed to exit the model domain through the "eastern" boundary northwest of Norway. The linear distribution is clearly arbitrary; no special provision was made to specify flow along the shelf edge, for example [e.g., *Huthnance*, 1984]. The amount of transport is deemed more important than its detailed variation along the boundary,

Table 2. Comparison of Model and Observation at Faroe-Shetland Channel

	Max U_n, m s^{-1}					
	Inflow	Outflow	$\delta_x T$, °C km^{-1}	$\delta_z T$, °C m^{-1}	$\delta_x U_n$, s^{-1}	$\delta_z U_n$, s^{-1}
Model	0.39	−0.22	0.05	6×10^{-3}	0.8×10^{-5}	3×10^{-4}
Observation	0.41	−0.17	0.12	16×10^{-3}	1.3×10^{-5}	5×10^{-4}

Max U_n is the maxima of velocity normal to the channel; $\delta_x T$ is the maxima of the cross-channel gradient of temperature; $\delta_z T$ is the maxima of the vertical gradient of temperature; $\delta_x U_n$ is the maxima of the cross-channel gradient of the normal velocity; $\delta_z U_n$ is the maxima of the vertical gradient of the normal velocity.

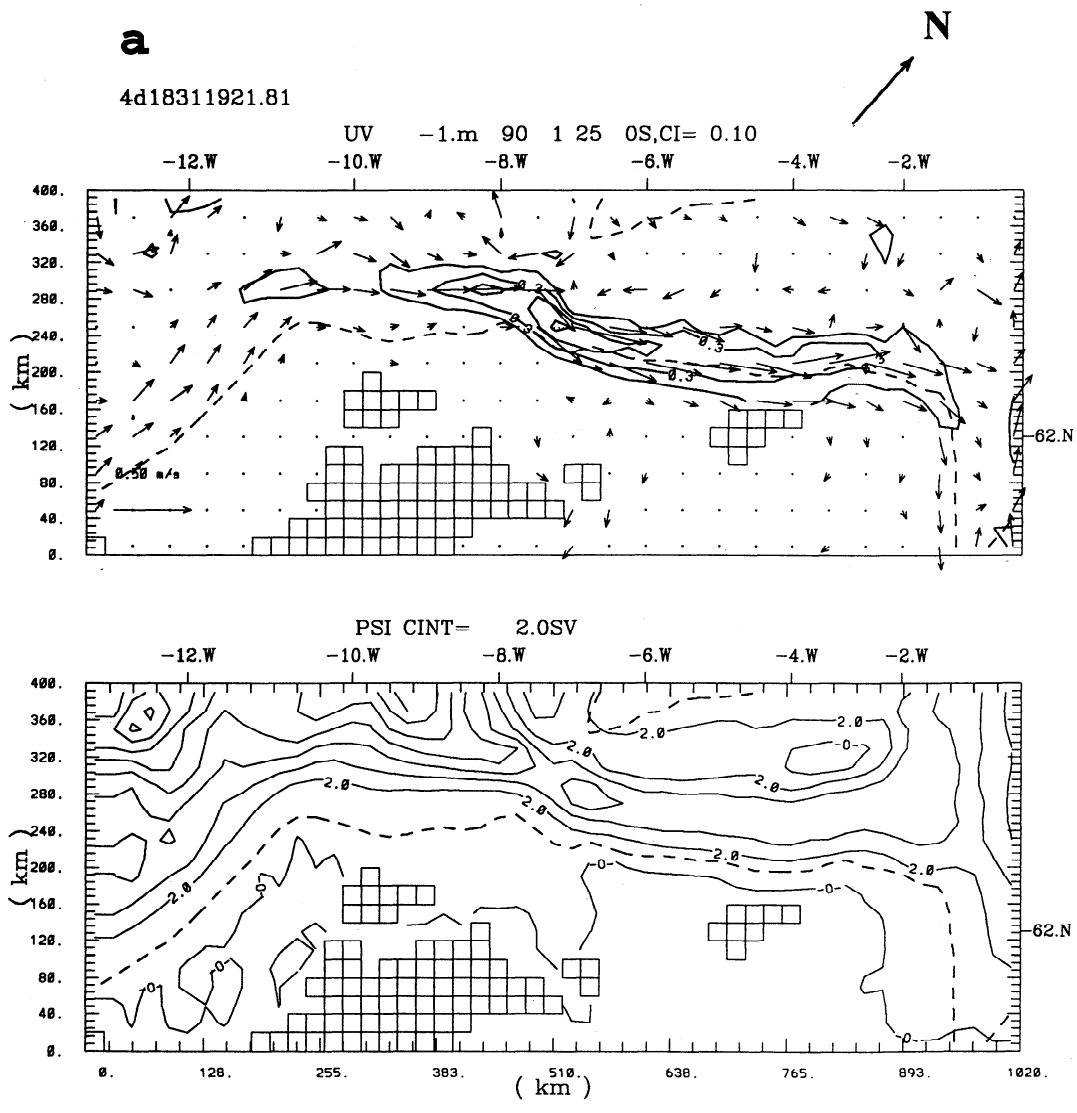

Figure 6. Vectors (with speeds contours, CI = 0.1 m s^{-1}, stippled where speeds exceed 0.5 m s^{-1}) and stream function (CI = 2 Sv, bottom panels) for (a) experiment 1 (no wind) and (b) experiment 0 (with wind).

since the interior circulation would adjust for the most part to the T/S field. (Recent experiments using various transport distributions have confirmed this.) Future work may consider specifying this detail from an even larger scale circulation model (the Atlantic Ocean model, for example). The three-dimensional velocities along all open boundaries except the western inflow boundary are allowed to adjust according to the interior flow field through the use of radiation conditions (OC). Along the western boundary a geostrophically balanced inflow profile is specified according to the specified total transport and the boundary temperature and salinity profiles. The latter along all open boundaries are obtained from *Levitus* [1982] and interpolated to monthly values. During inflow, Levitus' data are specified, while the temperature and salinity are advected using one-sided differencing during outflow. Free-slip conditions are used for tangential velocities along the open boundaries.

Tides are included in the simulation by specifying the amplitudes and phases of elevation and normal-component current of the four dominant tidal constituents, M2, S2, K1, and O1 [*Cartwright et al.*, 1980] along the open boundaries, using the iterative procedure of *Flather* [1976] (see also OC). The simulated tides (not shown) compare well with published charts [e.g., *Huntley*, 1980; *Davies et al.*, 1997].

3.3. Initial Conditions and Model Integration

The model was initialized with *Levitus*' [1982] T and S corresponding to December and run for 1 month (December 1–31, 1984) with all the forcing turned on except wind and atmospheric pressure. This field at December 31, 1984, was then taken as the initial condition, and integration was continued for 6 years through December 31, 1990. On the basis of the model basin length of 2000 km and the first-mode baroclinic Rossby wave phase speed of 0.05 m s^{-1}, the model spin-up time would be about 1–2 years (cf. OC). The sensitivity experiments (see below) were carried out for 1990, when integration had reached a quasi-equilibrium state. The model required 35-MB RAM, and the 6-year integration took about 500 hours on a 166-MHz DEC Alpha Station plus another 800 hours for nine 1-year sensitivity experiments. Model data archives including the sensitivity experiments totaled to about 20 GB.

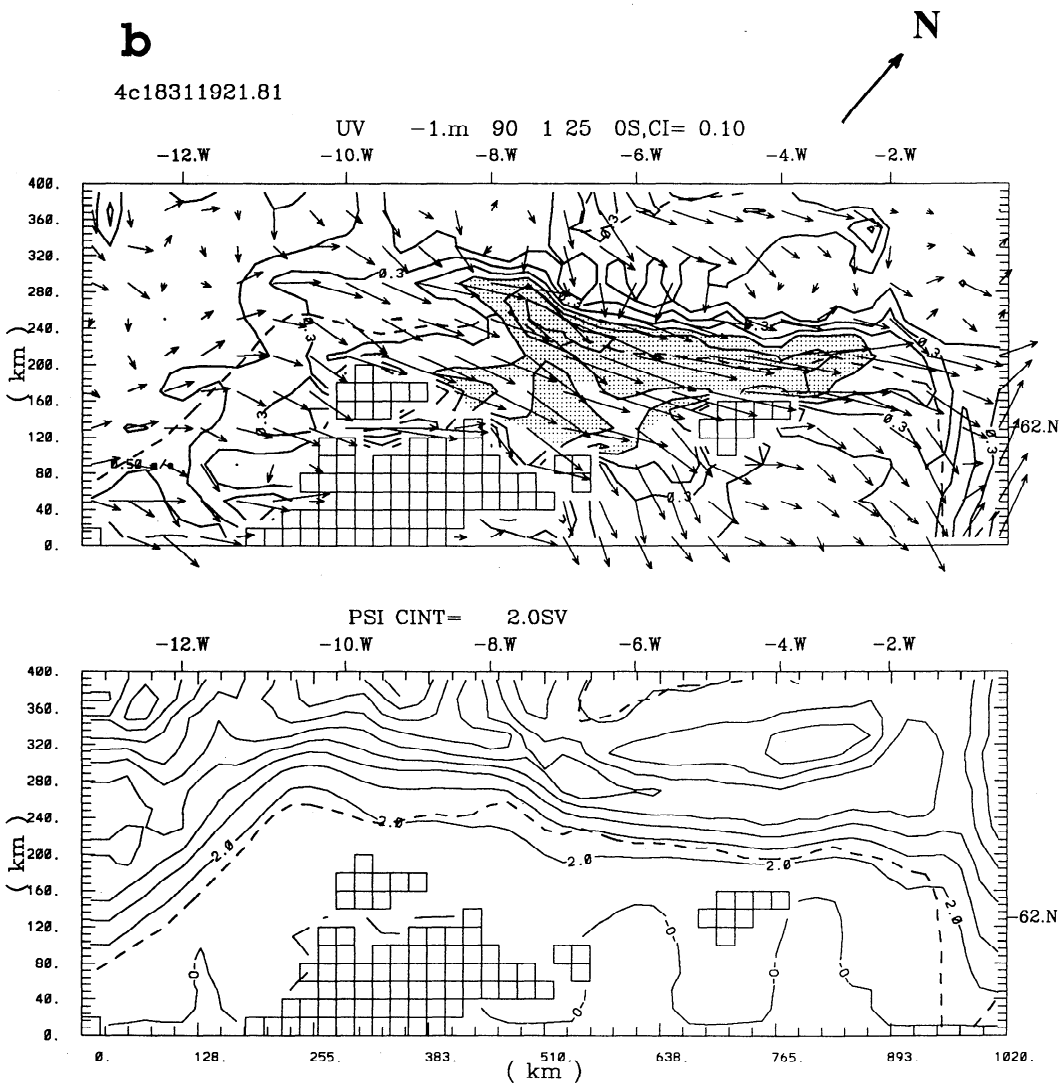

Figure 6. (continued)

3.4. Sensitivity Experiments

Table 1 lists the forcing and model parameters used in the basic experiment "0," as described above, as well as nine other sensitivity experiments. These experiments were initialized from the results of the basic experiment on December 5, 1989, and continued through December 31, 1990. For each experiment the change was made gradually (linear) over 20 inertial periods to reduce initial "shocks." Experiment 1 sets wind and atmospheric pressure to zero, and the difference between this and experiment 0 gives the wind- (and pressure-) induced solution. Experiment 2 will indicate effects of S2, K1, and O1 tides. Experiments 3 and 4 examine the sensitivity of the model solution to horizontal mixing; it will indicate also how much natural variability (i.e., that caused by dynamic instability, as opposed to wind forced, say) can exist at the 20-km grid. Experiments 5, 6, and 9 examine the importance of surface heat flux and atmospheric pressure, respectively, as these will likely contain error as input forcing. Similarly, experiments 7 and 8 examine the error incurred as a result of imperfect temperature and salinity fields and inflow transport along the open boundaries.

4. Results From the Basic Experiment 0

This section examines how the model's results compare with the overall circulation observed in the NWA, in particular, with *Saunders* [1990] data for the period May/June 1987. Figure 4 shows vectors and temperature contours at $z = -50$ m on May 25, 1987. (Unless otherwise stated, the model's results have been averaged over 2 days; the averaging eliminates most of the tidal signal yet retains the low-frequency wind-driven motions in the NWA.) The slope current is seen seaward of the 300-m isobath, with speeds of about 0.2 m s^{-1} south of the Wyville-Thomson Ridge (located at $x = 510$ km in Figure 4; see also Figure 2b) and over 0.3 m s^{-1} to the north. Peaks are 0.4 m s^{-1} just north of the ridge as the current turns abruptly shoreward. A filament of the warm North Atlantic water ($T > 10°C$) can be seen over the slope south of the Ridge and is clearly associated with the slope current. North of the ridge, the warm water is confined to the east while the cool Norwegian Sea water is to its north and west. This results in a stronger cross-slope temperature gradient north of the ridge, about 2°C per 100 km. These characteristics agree with the general observation features as summarized in section 2.

The vertical structures are shown in Figure 5b as contours of

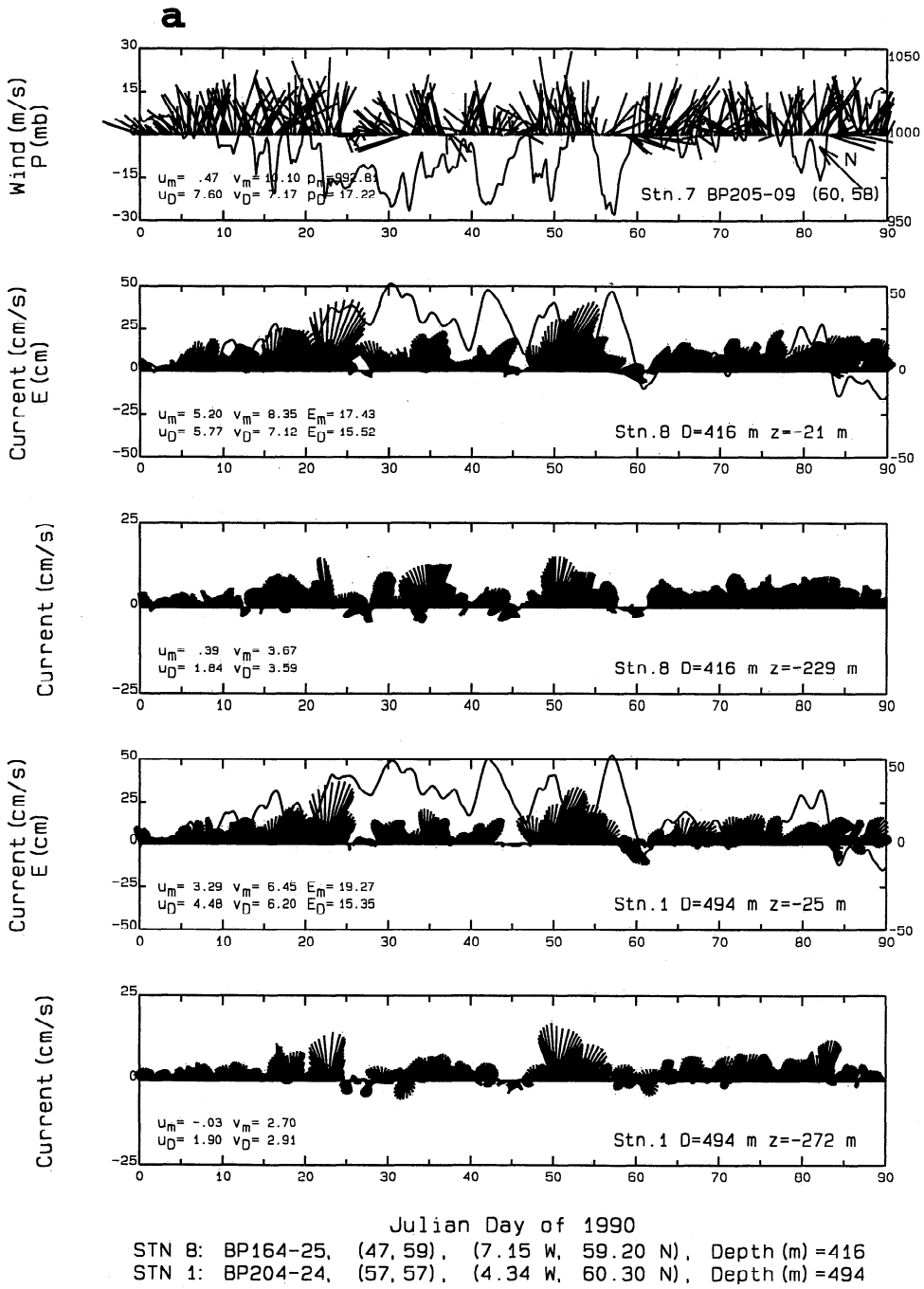

Figure 7. Wind (top panel) and wind-induced current stick plots for stations 8 (second and third panels) and 1 (fourth and bottom panels), experiment 0 (with wind) minus experiment 1 (no wind), for (a) January/February/March and (b) July/August/September 1990.

temperature and normal velocity U_n at the FSC section marked in Figure 2b and are compared with *Saunders'* [1990] conductivity-temperature-depth (CTD)/acoustic Doppler current profiler (ADCP) data (Figure 5a). Both model and observation show northward flowing ($U_n > 0$) warm water on the right side of the Faroe-Shetland Channel, with maximum surface speeds of the order of 0.4 m s^{-1}. (The model maximum is 0.39 m s^{-1}, reaching 0.43 m s^{-1} on May 27 (not shown) as the wind turned from northeasterly to southwesterly.) In the deep part of the Channel, flow is southward and bottom intensified, with speeds reaching 0.17 m s^{-1} (observation) and 0.2 m s^{-1} (model) near the bottom. Farther to the left of the channel, the model shows a predominantly northward flow, while observation shows what appears to be banded fine structures (northward then southward farther left of the channel). Both observation and model show updoming of the isotherms. However, observation shows $T < 0°C$ for waters at depths >600 m, while model's T ranges from 0° to 4°C. The model underestimates both the horizontal and vertical stratifications and also the velocity shears (Table 2). The more "diffused" modeled structures are a result of coarse horizontal grid, not the vertical mixing parameterization (*Oey* [1998]; see also the

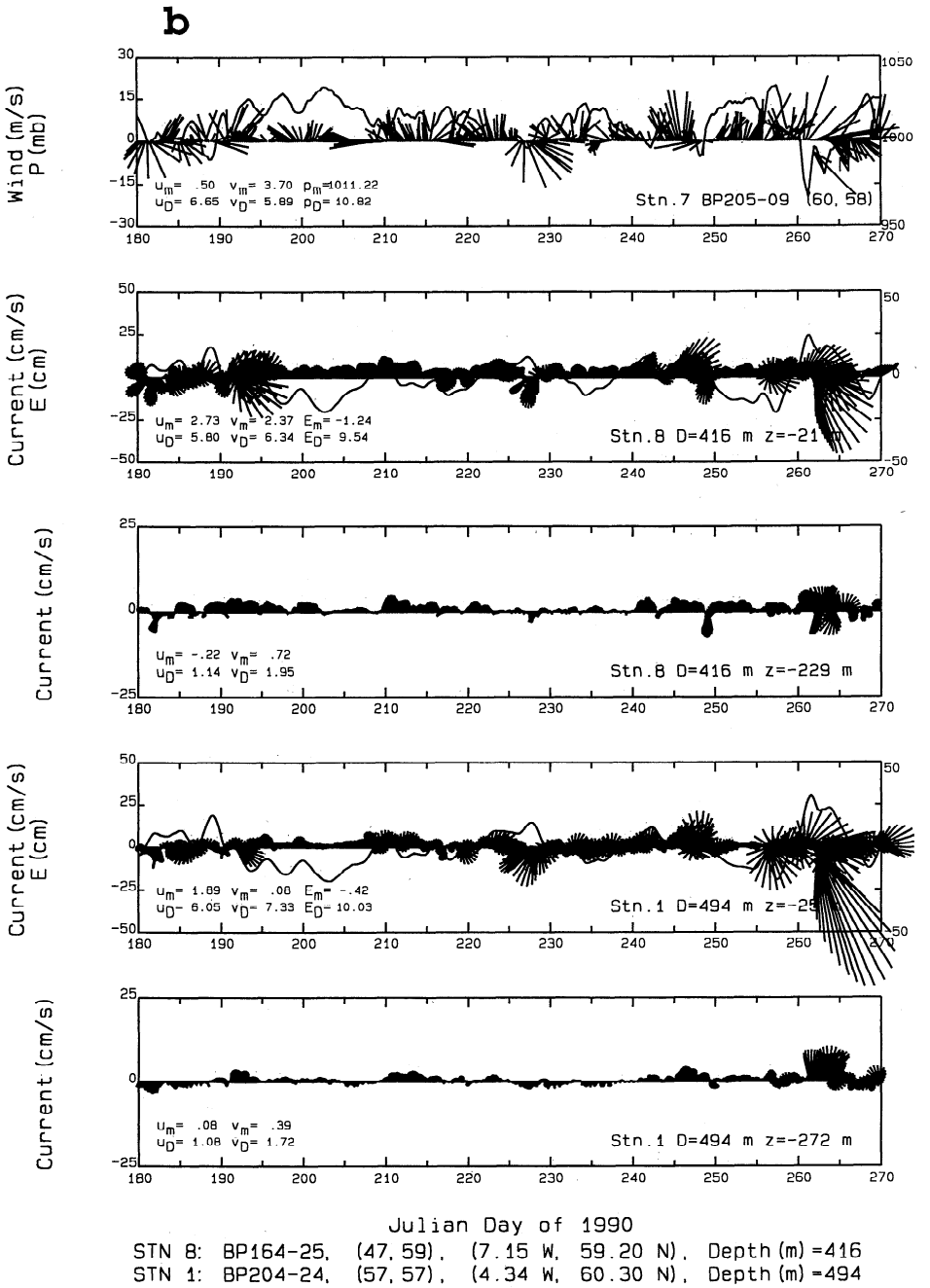

Figure 7. (continued)

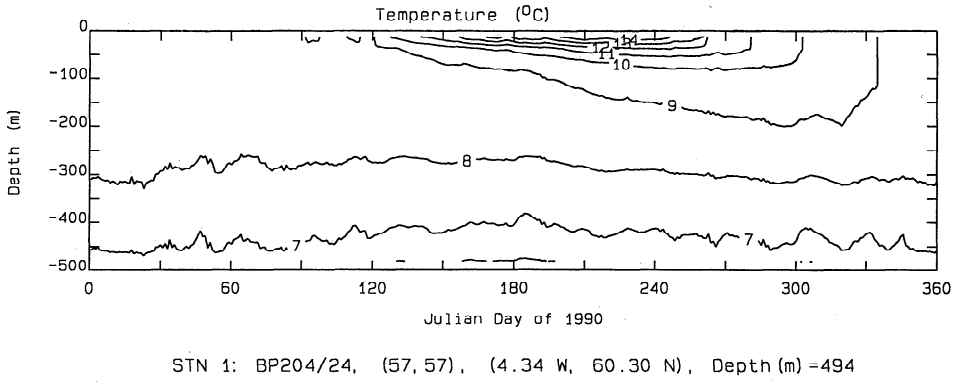

Figure 8. Time-depth contours of temperature at station 1 (CI = 1°C) for 1990.

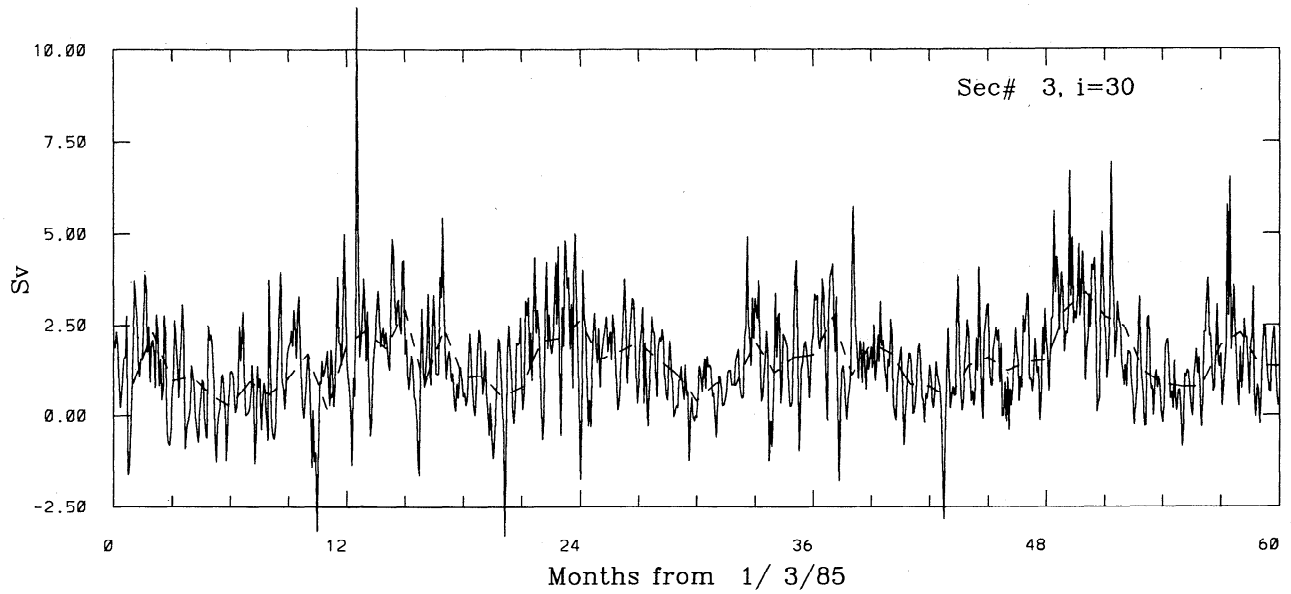

Figure 9. Five-year (1985–1989) time series of transport across the FSC section shown in Figure 2b. Solid line shows 2-day-averaged time series, and dashed line shows monthly averaged time series.

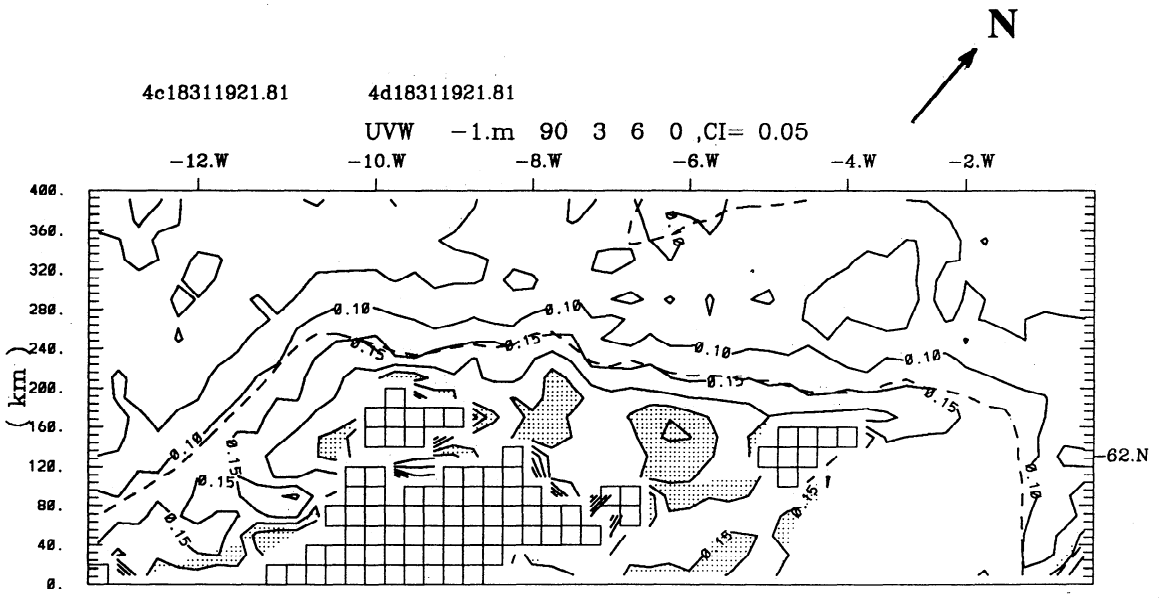

Figure 10. Effects of wind and variances of surface kinetic energy, experiment 0 minus experiment 1, with CI = 0.05 $m^2 s^{-2}$.

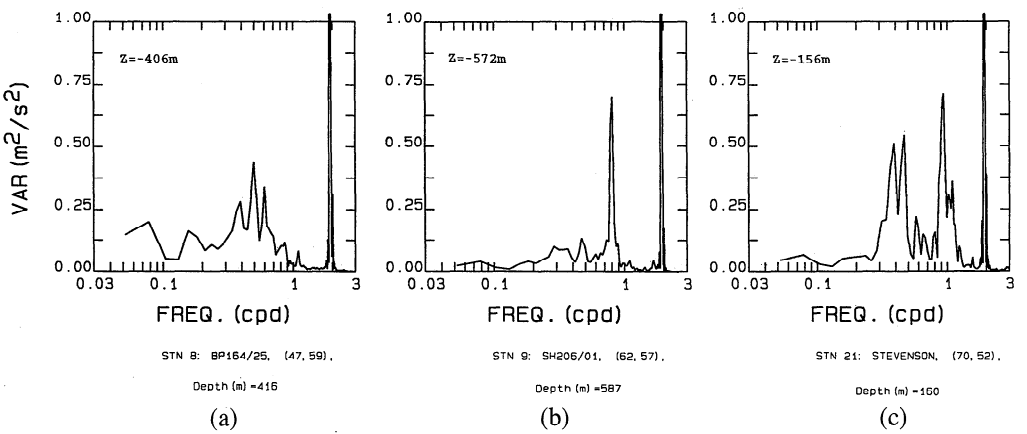

Figure 11. Spectra of near-bottom modeled currents for stations (a) 8, (b) 9, and (c) 21.

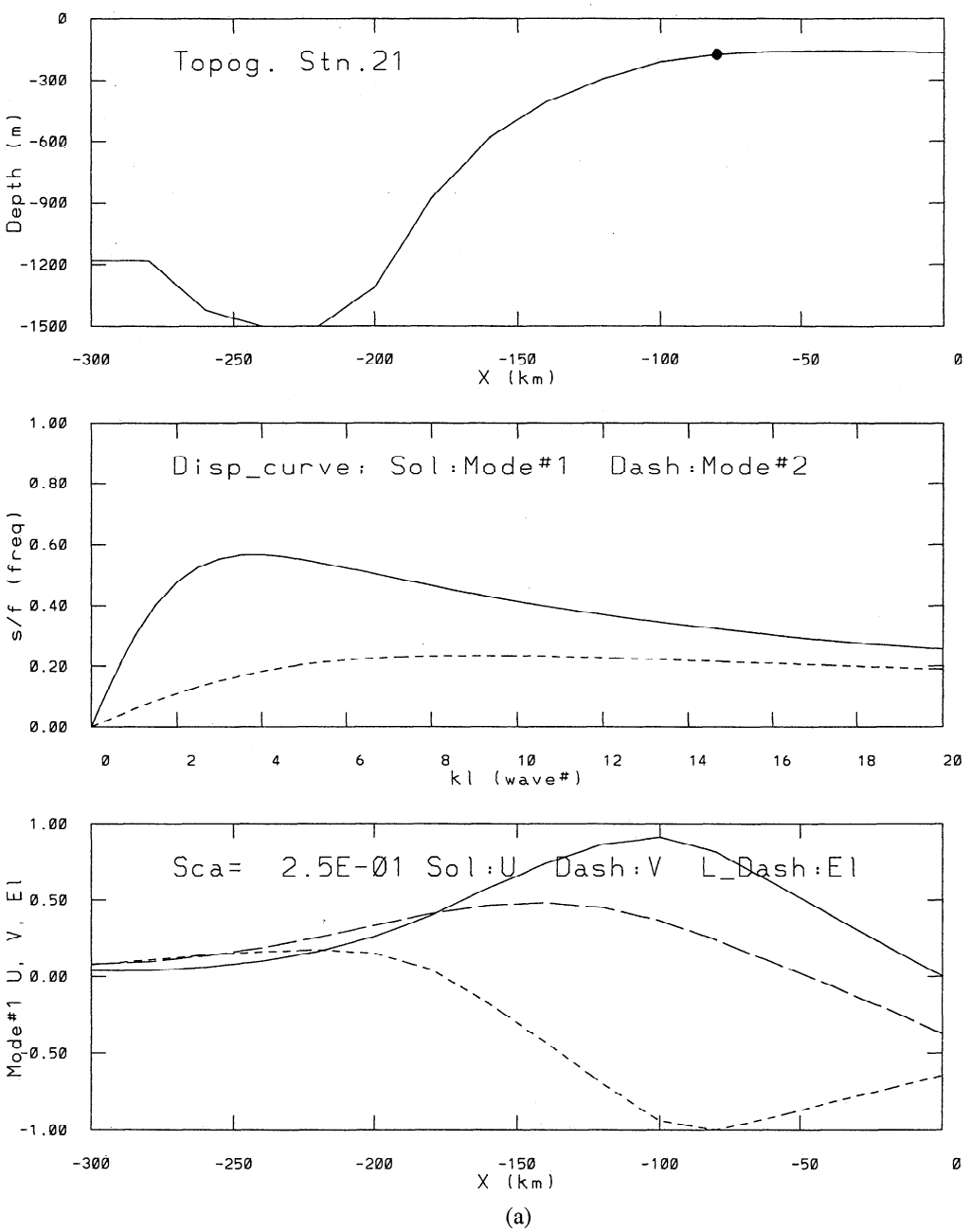

(a)

Figure 12. Depth profiles (top panels), dispersion curves (middle panels) and mode 1 U (cross-shelf velocity), V, and E (bottom panels) for stations (a) 21, (b) 9, and (c) 8. The solid dot on the depth profile indicates station location, l = 300 km, and the eigenfunctions are scaled by Sca = max$|V|$.

experiment with reduced mixing below). The upshot is that the modeled slope current is likely to be dynamically more stable, since flow instability depends on an adequate resolution of the velocity shears.

5. Sensitivity Experiments

Data from the Continental Slope Experiment (CONSLEX) indicate a mean slope current >0.3 m s^{-1} and along-slope and cross-slope standard deviations of about 0.1 and 0.04 m s^{-1}, respectively [*Huthnance*, 1986]. Thus the current is dominated by its mean. The currents' variance is due in part to natural variability of the flow (via dynamical instability, for example) and in part forced variability. Only the low-frequency response (i.e., 2 days averaged) is considered here.

5.1. Effects of Wind (Experiment 1)

By far the most visible response in the simulation is that caused by winds. Here the response is examined in more detail and related to published observations. Figure 6 shows an example of vectors and stream functions (transports) for experiments 1 (without wind; Figure 6a) and 0 (with wind; Figure 6b) on January 25, 1990, near the end of a period of intense northeastward wind (maximum speed ≈30 m s^{-1}; Figure 3). Figure 6a shows that the acceleration of the slope current north of the Wyville-Thomson Ridge is bathymetrically in-

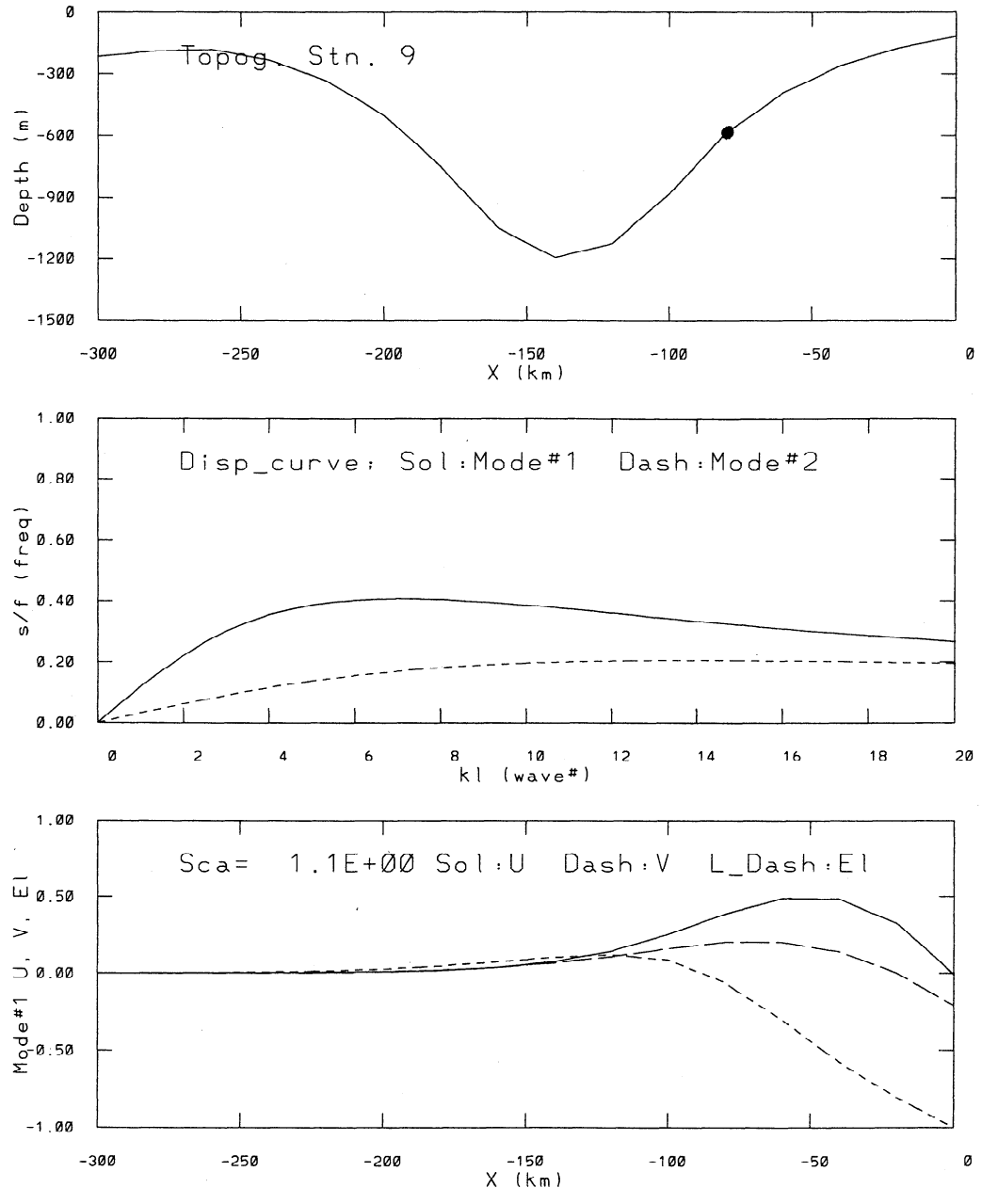

(b)

Figure 12. (continued)

duced independent of the wind; speeds exceed 0.4 m s^{-1}, and transport is about 4 Sv. With winds (effects of atmospheric pressure at low frequencies are small; see below), Figure 6b shows peak transports of 7–8 Sv and current speeds that exceed 0.7 m s^{-1} just downstream of the ridge. In the following, wind effects are discussed by subtracting experiment 1 from experiment 0.

Figure 7 shows vector stick plots just inshore of the 500-m isobath at stations 8 and 1, upstream and downstream, respectively, of the Wyville-Thomson Ridge, for periods January–March (Figure 7a) and July–September (Figure 7b) of 1990, at the near-surface ($z \approx -25$ m) and middepth ($z \approx -250$ m) levels. There is a good visual correlation between wind and currents, as well as coherence in the currents' response between the station pair (indicative of the extent of the wind forcing). The response is quasi-steady in that the current amplitude increased as long as the wind blew and stopped when the wind stopped (i.e., the type 2 response of *Gordon and Huthnance* [1987]). In winter (Figure 7a) the response extends to the middepth (~200 m) while summertime response is restricted near the surface (Figure 7b). This relates to the seasonal stratification which indicates (Figure 8) a complete breakdown in the upper 300 m from December through April. A consequence of this is that the near-surface gain factor (GF) (GF is the currents' speeds per unit wind speed) in summer is as much as 3 times the winter value. An example is seen in Figure 7b around day 262 (September 20) when an intense cyclone with 25 m s^{-1} southeastward (peak) wind generated peak currents with speeds of 0.8 m s^{-1} at station 1, so that GF ~ 3% (GF ~ 2% for station 8), compared to Figure 7a

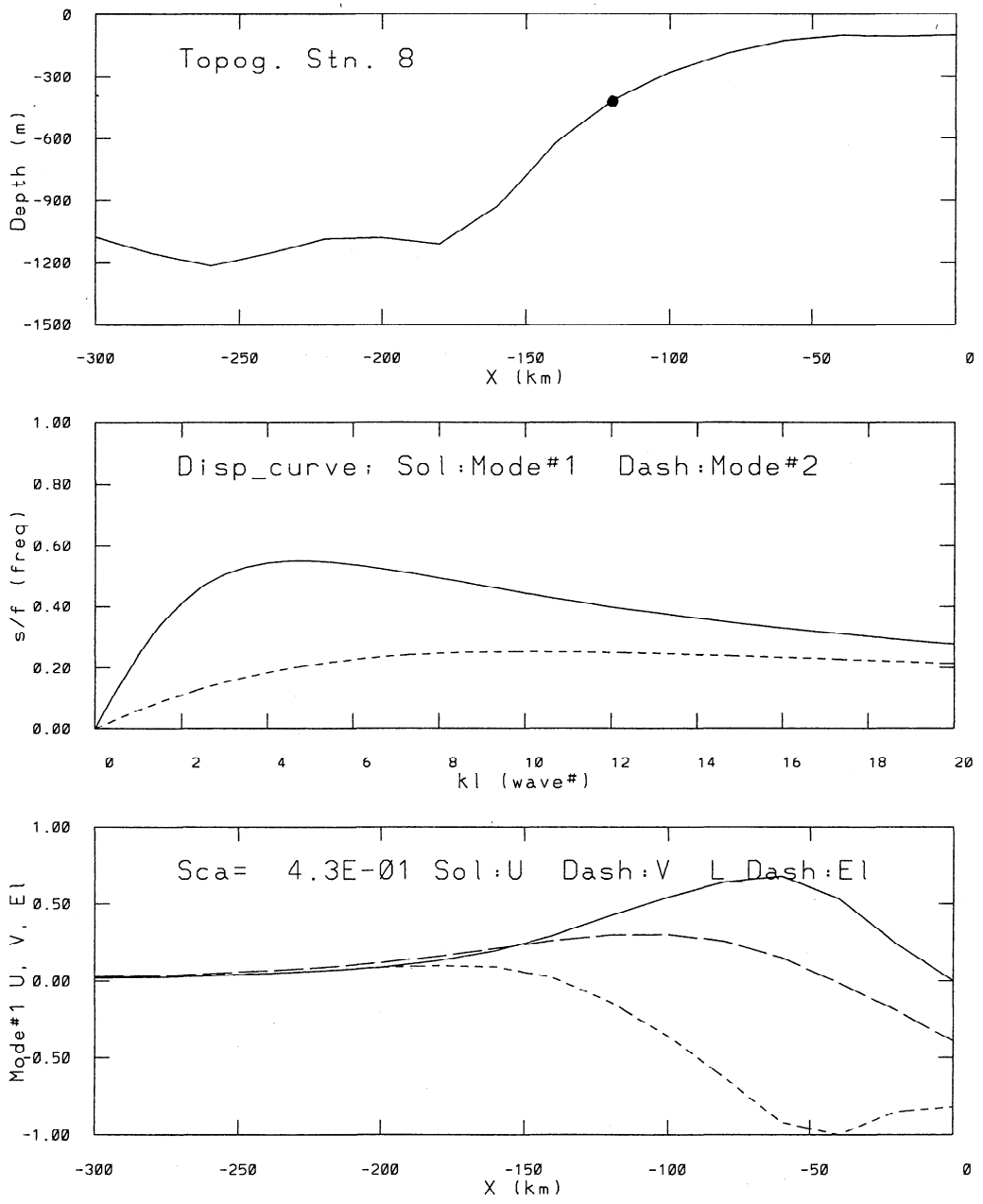

(c)

Figure 12. (continued)

around day 51 (February 20) with GF ~ 1% (GF ~ 1.5% for station 8). That stratification accounts for the different response was confirmed by running the model in a one-dimensional (vertical) diagnostic mode at station 1, using the background temperature profile shown in Figure 8 and forcing by the same 1990 wind.

The majority of storms occur in winter, and their tracks are from west/southwest to east/northeast with (cyclone) centers passing approximately over the Iceland-Faroe ridge, so that wintertime winds over the channel generally blow in an east/northeastward (i.e., "downstream") direction (Figure 3). One expects that the resulting sea level setup would, in general, lead to an increased northeastward transport (Figure 6). Figure 9 shows 5-year (1985–1989) time series of transport across the FSC section shown in Figure 2b. In addition to the large fluctuations (amplitudes > 2 Sv, periods ~14 days) that occur primarily during the winter months, the monthly averages (dashed) show a clear cycle of winter maximum that reaches 3 Sv and a summer minimum of about 0.3 Sv. These variations are almost entirely wind induced, since the experiment 1 (without wind) shows an almost steady transport of a little <2 Sv (Figure 6a). The annual cycle may be compared with estimates derived from satellite altimetry data by *Samuel et al.* [1994], which also showed winter peaks and summer lows (1987 through 1989) with a mean of about 2.5 Sv and fluctuation amplitude of about 2 Sv. Their higher mean and fluctuation amplitudes (by 0.8 and 0.7 Sv, respectively) are in part because altimetry data give estimates of the near-surface transport only, whereas Figure 9 gives the total transport. The model suggests then that a portion of the observed annual variation in transport is wind induced. Moreover, the wind-induced, wintertime (January/February/March; Figure 10), near-surface current fluctuations are of $O(0.2\ \text{m s}^{-1})$ on the shelf and about 0.05–0.1 m s^{-1} in the channel. The alongshore and

Table 3. Shelf Wave Characteristics at Stations 21, 9, and 8

Station Number	Grid Description	Mode 1 Period hours	Mode 1 Wavelength, km	Mode 2 Period hours	Mode 2 Wavelength, km	3-D Model P_{3D},* hours
21	Δ = 20 km	24.5	471	59.2	221	23–25
	Δ = 10 km	23.3	538	60.2	235	
9	Δ = 20 km	34.0	269	67.2	145	30
	with shelf	22.9	471	52.5	198	
	Δ = 10 km	25.3	251	67.6	118	
8	Δ = 20 km	25.2	419	55.0	188	23, 28
	next grid	27.1	377	60.0	188	
	Δ = 10 km	20.5	419	54.3	114	

*P_{3D} is the period that corresponds to the near-diurnal peaks of the spectra (Figure 11) obtained from the three-dimensional (3-D) model result.

Here Δ denotes grid size used in the analysis.

cross-shore current variances (not shown) in the channel are 0.1 and 0.05 m s^{-1}, respectively. These agree with CONSLEX and suggest that wind-induced motions make up a substantial portion of the current fluctuations, especially in winter.

Gordon and Huthnance [1987] describe resonance continental shelf wave with a period of about 23 hours. The wave has zero group velocity and is "trapped" in the channel because decreased bottom slopes north and south over the Norwegian Trench and Wyville-Thomson Ridge allow propagation of only longer waves. The waves were forced by relatively short-duration winds (typically a half day). To search for this near-diurnal signal, energy spectra of experiment 2 (which excludes diurnal tides) at one grid cell above the bottom were examined. Figure 11 shows examples at stations 8 (upstream of the

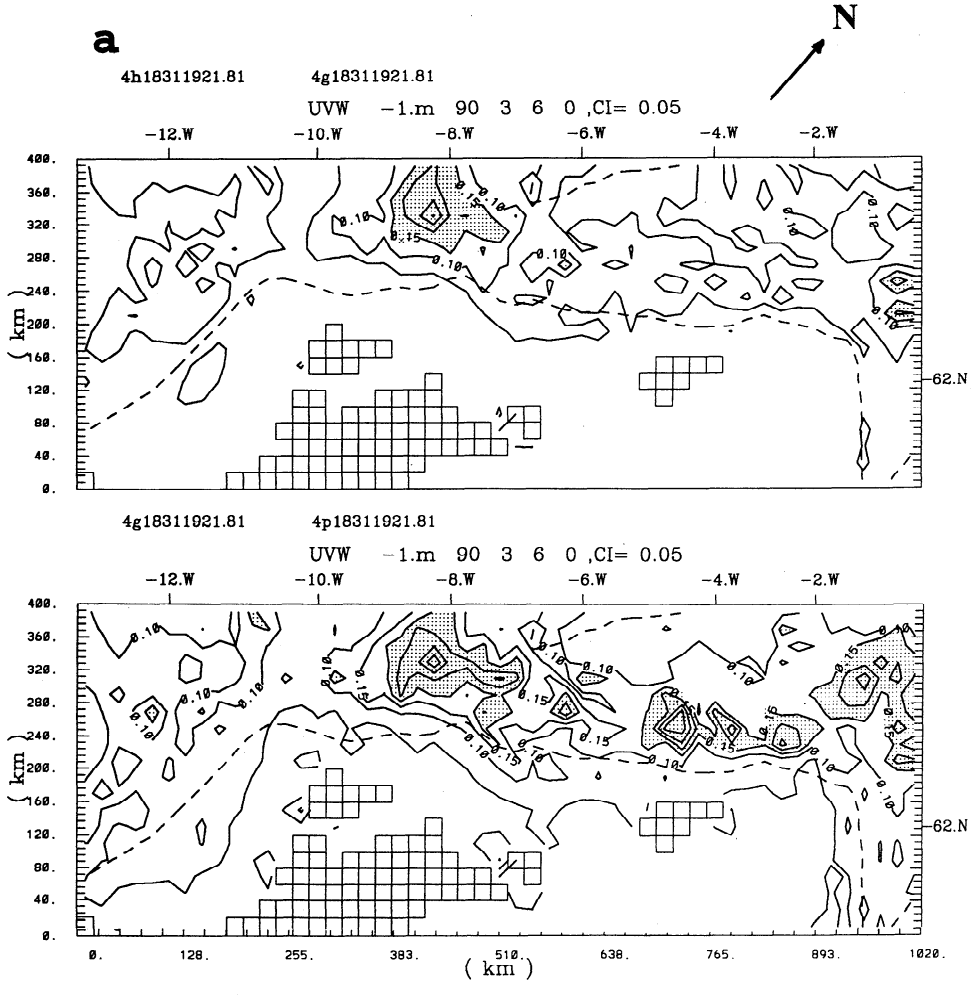

Figure 13. Effects of horizontal viscosity/diffusivity, C, decreased from 0.2 to 0.1 (top panels, experiment 3 minus experiment 0) and from 0.2 to 0.05 (bottom panels, experiment 4 minus experiment 0). Variances of (a) surface kinetic energy (CI = 0.05 m^2 s^{-2}) and (b) temperature (CI = 0.2°C^2).

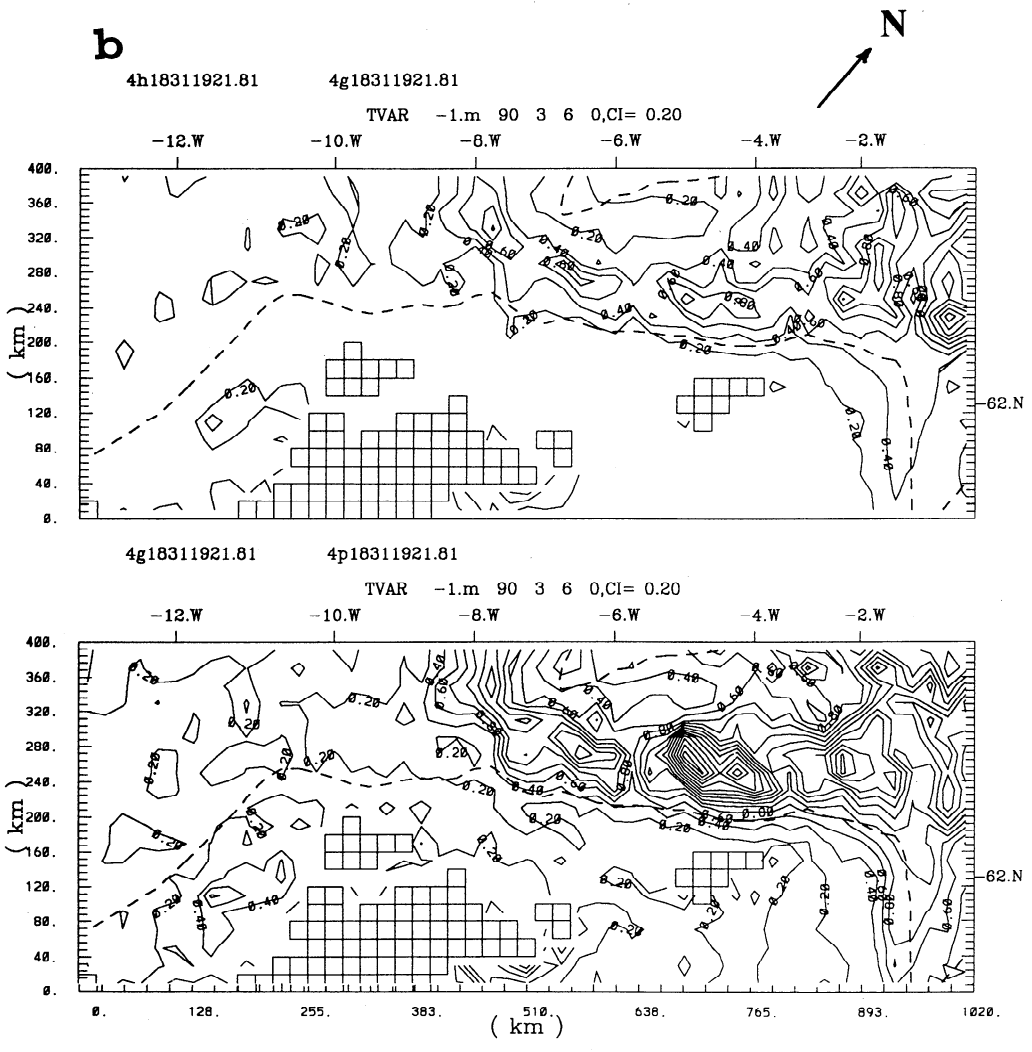

Figure 13. (continued)

Wyville-Thomson Ridge), 9 (downstream, over slope), and 21 (downstream, on shelf at Stevenson; see Figure 2b, station 21). Periods of the peaks are $P_{3D21} \approx 23$–25 hours at station 21, $P_{3D09} \approx 30$ hours at station 9, and $P_{3D08} \approx 23$ and 28 hours at station 8 (P is period, subscript denotes three-dimensional model and station number). More detailed analyses (not shown) revealed that the response has a significant barotropic component that extends to the near surface and also that the currents have many of the resonance shelf wave characteristics, including clockwise rotation with the along-slope component leading the onshore component by 90°. To examine if the near-diurnal periods in the spectral peaks correspond to the resonance shelf wave periods, dispersion relations at cross-shelf transects that pass through each station are obtained by solving the following eigenvalue problem [*Cartwright et al.*, 1980; *Heaps et al.*, 1988]

$$(hE_x)_x + E[(s^2 - f^2)/g - hk^2 - fkh_x/s] = 0 \qquad (8a)$$

$$sE_x - fkE = 0 \qquad x = 0 \qquad (8b)$$

$$E \to 0 \qquad x \to -\infty \qquad (8c)$$

Here E is the elevation eigenfunction; s is the frequency; f = Coriolis parameter = 1.26×10^{-4} s^{-1}; k is the wave number; x is the cross-shore coordinate with the coast (Scotland), taken as $x = 0$ where no-flow condition (8b) is imposed, negative x points away from the coast so that the solution is required to decay away from the coast (condition (8c)); and $h(x)$ is the cross-shelf depth profile. Equation (8a) is solved by writing it as two first-order differential equations, integrating onshore from an exponential decaying form (multiplied by an arbitrary amplitude of 1) in the constant-depth offshore region, and searching in the s-k space such that (8b) is satisfied. Figure 12 shows the depth profiles (top panels), dispersion curves (middle panels), and mode 1 U (cross-shelf velocity), V, and E (bottom panels) for stations 21 (Figure 12a), 9 (Figure 12b), and 8 (Figure 12c), and Table 3 shows the numerical values. At station 21 the mode 1 resonance period P_{sw21} (subscript "sw" denotes shelf wave model based on (8)) of 24.5 hours agrees with P_{3D21} (Table 3). With a higher-resolution topography on a 10-km grid (not merely interpolating from the 20-km grid topography, which did not significantly change the result), P_{sw21} is reduced to about 23 hours in better agreement with the values reported by *Heaps et al.* [1988]. This improvement is true also at other stations (Table 3), which favors the use of a more refined topography as noted by *Proctor and Davies* [1996]. The eigenfunction plots in Figure 12a shows, moreover, that station 21 is located where the shelf wave response is near its maximum, consistent with the large spectral peak of Figure 11. At station 9, $P_{sw09} = 34$ hours $> P_{3D09} = 30$ hours, but they are consistent in that both are longer than diurnal, suggesting a common underlying cause. Improving the topography (Δ = 10 km) or extending onshore with a constant-depth shelf (92.5 m and 80 km wide) lowers P_{sw09} to near diurnal (Table 3) and

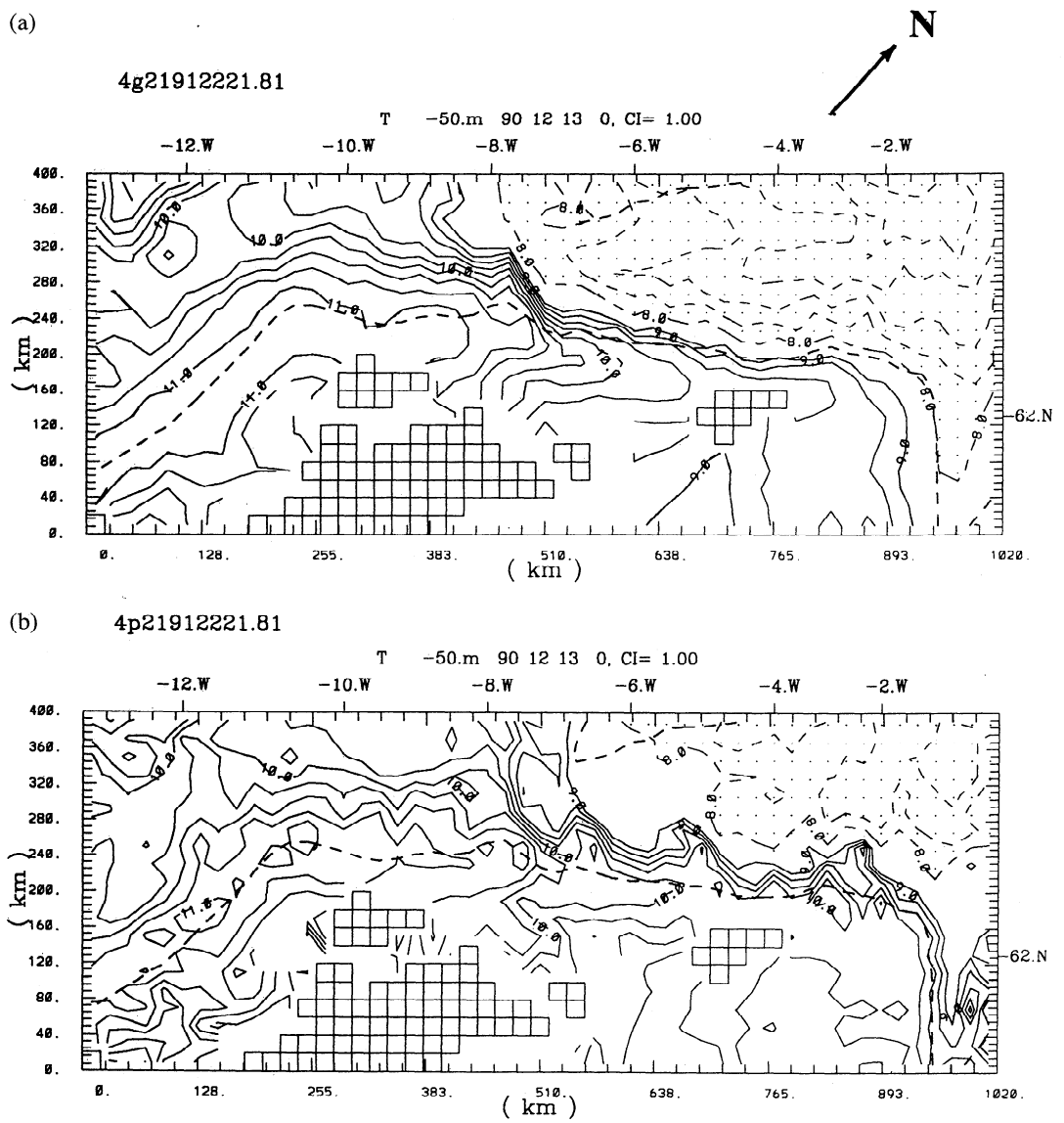

Figure 14. Modeled temperatures at $z = -50$ m on December 13, 1990, for (a) experiment 0 (base experiment) and (b) experiment 4 (reduced horizontal viscosity and diffusivity). CI = 1°C.

also decreases the apparently large response (note that the V scale is 1 m s^{-1} in Figure 12b, largest of the three stations) by 50% for an 80-km-wide shelf (not shown). Thus the longer resonance period depicted by the three-dimensional model at station 9 and the apparently large response (Figure 11) are artifacts of poor bathymetric resolution that omit the shallow shelf and steep gradient slope northwest of Shetland Islands (Figure 2). At station 8, $P_{sw08} = 25$ hours is closer to the higher-frequency peak (period ~23 hours) of the two near-diurnal peaks of P_{3D08} of Figure 11. The assumption of along-shelf invariance (inherent in (8)) is not strictly valid in this region, however, because of diverging isobaths near the Wyville-Thomson Ridge, and P_{sw08} (as well as other shelf wave characteristics) is found to vary significantly from one alongshore grid to the next (Table 3). The existence of another spectral peak at $P_{3D08} = 28$ hours may therefore be attributed to this alongshore nonuniformity of the shelf wave properties. Also, the linear model predicts a small response consistent with the small spectral peaks in Figure 11, since station 8 is located where shelf wave amplitudes begin to decay on the slope (Figure 12c).

In summary, the 23–30-hour spectral peaks found in the three-dimensional model result (Figure 11) are resonance shelf wave responses. Departures from near-diurnal (~23 hours) response are due to poor bathymetric resolution (with $\Delta = 20$ km grid) and alongshore nonuniformity.

5.2. Effects of Horizontal Viscosity and Diffusivity (Experiments 3 and 4)

I subtract experiment 0 from experiments 3 and 4 and compute standard deviations. Examples are given in Figure 13a, which compares values for the near-surface currents, and Figure 13b, which compares values for temperatures. Smaller values of the horizontal viscosity and diffusivity (experiment 4, bottom panels of Figure 13) lead to larger current variances at the expense of the mean flow, since the energy inputs (from winds, tides, and inflows, etc.) remain the same. The largest increase occurs over the Wyville-Thomson Ridge and near the Faroe Bank Channel as the slope current makes an abrupt east/northeastward turn. There is also increased variance in the NWA region in the FSC. The smaller viscosity/diffusivity also

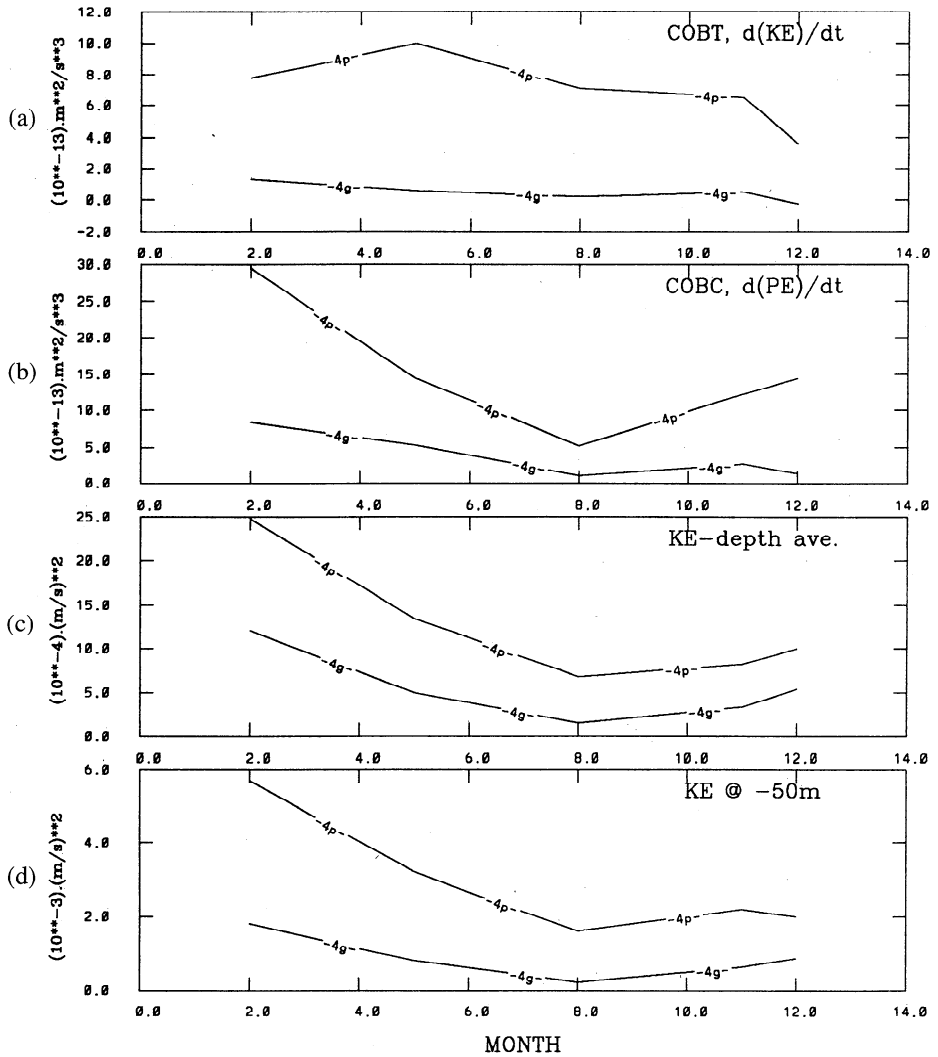

Figure 15. Barotropic and baroclinic growth rate of (a, b) eddy energies and kinetic energies (c) of the depth-averaged velocity and (d) of currents at $z = -50$ m for experiments 4 (reduced horizontal viscosity and diffusivity) (marked "4p") and 0 (marked "4g"), as functions of months of year in 1990.

results in increased temperature variance (Figure 13b) caused by current meanders, with typical wavelengths of about 100 km (Figure 14b). Calculations of both the barotropic and baroclinic instability sources show increased energy production as viscosity and diffusivity are reduced (Figure 15), which suggest that the slope current may be dynamically unstable. There is then the question of whether or not the physics that lead to these enhanced eddy activity are fully accounted for on a $\Delta =$ 20 km grid. A convergence study (eddy energetics as a function of grid sizes [*Oey*, 1998]) shows that they are not, primarily because the intense shears of the slope current are not adequately resolved. Moreover, at fine grid sizes $\Delta \sim 2$ km or less, the eddy solution becomes insensitive to the horizontal mixing (with Smagorinsky constant $C \sim 0.1$). Thus, while the coarse grid can support the mean flow [*Oey*, 1998], only a portion of the eddy variability is resolved (the meander in Figure 14b is not 2Δ-wave), and the relative sensitivity to horizontal mixing is an artifact of the coarse grid.

5.3. Other Effects and Summary

Increasing the inflow (from 5 to 10 Sv; experiment 8) produces a primarily barotropic response in that currents increase with small shears (5 cm s^{-1} per 500 m) from surface to $z = -1000$ m and transport in the channel is approximately doubled. Shutting off the heat flux (experiment 5) has the largest effect in the sea surface temperature (SST) (becoming 1.6°C warmer in winter and 3°C cooler in summer) and hence also in the seasonal thermocline and the upper layer currents. The change in currents is about 0.05 m s^{-1} near the surface and about 0.02 m s^{-1} at $z = -200$ m.

Figure 16 summarizes the percentage change in the kinetic energy (KE) for various experiments, measured with respect to the KE of experiment 1 (inflow plus tides only). Of the remaining experiments, significant changes in the currents occur only for the case when lateral T and S are changed (experiment 7), as can be expected since the slope current depends on the north/south gradient in density and hence also on the boundary T and S. The change is rather small, however, and only results in about a 0.2 Sv decrease in the along-slope transport (in the channel). The reason is in part because the model also depends on the oceanic density (hence T/S) field indirectly via the total transport at the inflow boundary, which was kept fixed. The effects of atmospheric pressure and surface relaxation are insignificant and so are the effects of S2, K1, and O1 tides

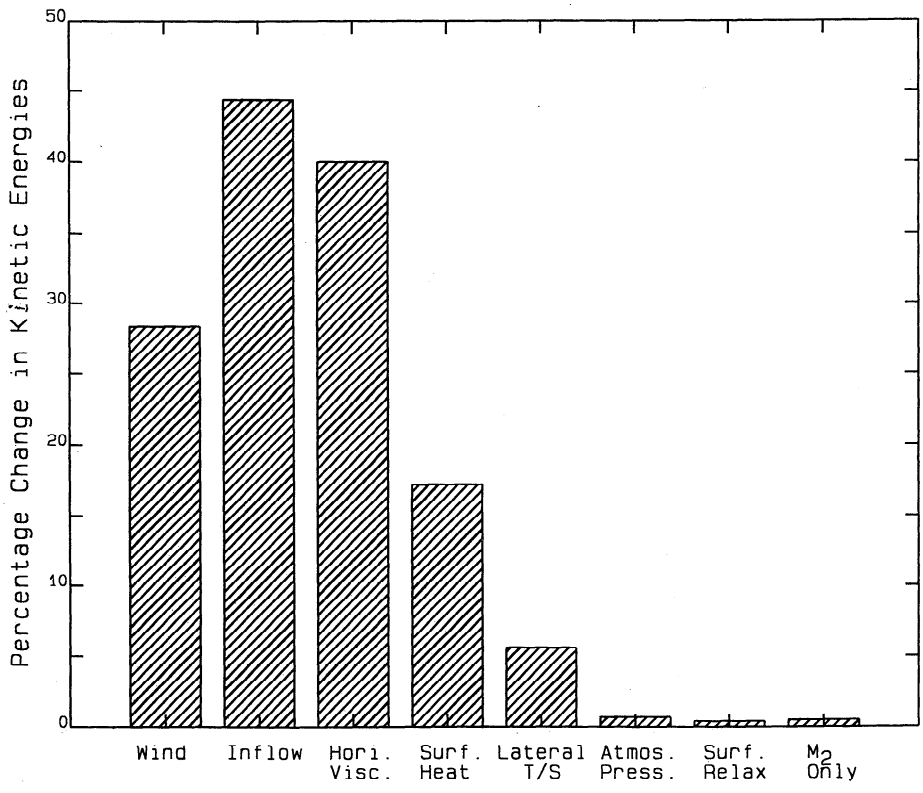

Figure 16. Percentage change in kinetic energies at $z = -50$ m, averaged over the NWA region between 200- and 1000-m isobaths and over the year 1990, for various experiments. Changes are relative to experiment 1 (inflow plus tides only), the kinetic energy of which is 3.8×10^{-2} m^2 s^{-2}.

(experiment 2) on the low-frequency variability over the slope and deeper. Although the S2 tidal current can be as much as 30% of the M2, its contribution to the energy dissipative process and mixing is smaller, proportional to $0.5[(M2 + S2)^3 + (M2 - S2)^3]/M2^3$, i.e., to the square of the S2/M2 ratio. However, the spring neap cycle that results does have effects on the shelf, especially during the summer (not shown).

6. Concluding Summary

A time-dependent three-dimensional simulation of the NWA circulation has been conducted, forced by winds from 1985 through 1990; M2, S2, K1, and O1 tides; monthly surface heat fluxes; and monthly lateral (boundary) T and S derived from *Levitus*' [1982] data. The simulation reproduces the observed large-scale features of the circulation in the NWA region, including surface-intensified northward flow of the warm and saline North Atlantic water on the right side (looking north) of the FSC and bottom-intensified outflow of the cold and less saline Norwegian water to the left and in the deeper part of the channel. There are, however, discrepancies in the magnitudes of the velocity and values of the temperature. The model gives weaker stratification and velocity shears and also less structures than those observed.

Winds produce large current and transport variabilities that account for a significant portion of the observed low-frequency variance (CONSLEX data). The model also shows spectra peaks at periods of about 23–30 hours for stations between the Wyville-Thomson Ridge and the Norwegian Trench. This agrees with the observations and theory of *Gordon and Huthnance* [1987], which show the existence of resonant continental shelf wave mode with period of about 23 hours. The longer period in the simulation is a result of coarse bathymetric resolution used.

Various experiments were conducted to assess the sensitivity of the simulation on model forcing and parameters (Table 1 and Figure 16). In particular, the model solution was sensitive to changes in the values of the horizontal viscosity and diffusivity, in that the eddy kinetic energy increased (caused by currents' meanders) when viscosity and diffusivity were reduced. Although the meanders appeared to be structured (i.e., not grid-scale noise, Figure 14), suggestive of dynamical instability of some sort, it is likely that there exits significant (eddy) energies at scales which are not resolved by the 20-km grids. Satellite images often show meanders with 10–30-km scales downstream of the Wyville-Thomson Ridge, which would suggest grid resolution of the order of 1 km. This topic is taken up by *Oey* [1998].

Increased lateral transport primarily results in a barotropic current response. However, increases in the lateral as well as vertical shears are fairly significant. Since these may contribute to meander and eddy production via dynamical instability, more realistic simulations may require time-varying transport specifications rather than the steady value used here. Finally, the model is fairly sensitive to surface heat flux forcing (about 16% change in KE) and less sensitive to details of the T and S specifications along the lateral boundaries (provided that the total transport is of the "correct" order of magnitude). This latter finding is important, since boundary T and S are the least known variables in the model forcing.

Acknowledgments. This research was supported by the Northwest Approaches Group. I am indebted to Jim Bole and Colin Grant for

encouragements, to Cort Cooper for constructive criticisms, and to Dave Peters for alerting me of the work of *Samuel et al.* [1994]. I am grateful to Alan Davies and John Huthnance for reviewing an earlier draft. Thanks to Jeff Ji and Alan Blumberg for drafting some of the figures.

References

Booth, D. A., Eddies in the Rockall Trough, *Oceanol. Acta*, *11*, 213–219, 1988.

Booth, D. A., and D. J. Ellett, The Scottish Continental Slope Current, *Cont. Shelf Res.*, *2*(2/3), 127–146, 1983.

Bunker, A. F., Computations of surface energy flux and air-sea interaction cycles of the North Atlantic Ocean, *Mon. Weather Rev.*, *104*, 1122–1140, 1976.

Cartwright, D. E., A. G. Edden, R. Spencer, and J. M. Vassie, The tides of the northeast Atlantic Ocean, *Philos. Trans. R. Soc. London, Ser. A*, *298*, 87–139, 1980.

Cummins, P., and L.-Y. Oey, Simulation of barotropic and baroclinic tides off northern British Columbia, *J. Phys. Oceanogr.*, *27*, 762–781, 1997.

Davies, A. M., S. C. M. Kwong, and R. A. Flather, A three-dimensional model of diurnal and semidiurnal tides on the European shelf, *J. Geophys. Res.*, *102*, 8625–8656, 1997.

Dickson, R. R., W. J. Gould, C. Griffiths, K. J. Medler, and E. M. Gmitrowicz, Seasonality in currents of the Rockall Channel, *Proc. R. Soc. Edinburgh, Sect. B, Biol. Sci.*, *88*, 103–125, 1986.

Dooley, H. D., and J. Meincke, Circulation and water masses in the Faeroese Channels during OVERFLOW '73, *Dtsch. Hydrogr. Z.*, *34*, 41–55, 1981.

Dooley, H. D., J. H. A. Martin, and R. Payne, Flow across the continental slope off northern Scotland, *Deep Sea Res. Oceanogr. Abstr.*, *23*, 875–880, 1976.

Ellett, D. J., A. Edwards, and R. Bowers, The hydrography of the Rockall Channel—An overview, *Proc. R. Soc. Edinburgh, Sect. B, Biol. Sci.*, *88*, 61–81, 1986.

Flather, R. A., A tidal model of the northwest European continental shelf, *Mem. Soc. R. Sci. Liege Coll. 8*, *6*(10), 141–164, 1976.

Gill, A. E., *Atmosphere-Ocean Dynamics*, 662 pp., Academic, San Diego, Calif., 1982.

Gordon, R. L., and J. M. Huthnance, Storm-driven continental shelf waves over the Scottish continental shelf, *Cont. Shelf Res.*, *7*, 1015–1048, 1987.

Heaps, N. S., J. M. Huthnance, J. E. Jones, and J. Wolf, Modelling of storm-driven shelf waves north of Scotland, 1, Idealized models, *Cont. Shelf Res.*, *8*, 1187–1210, 1988.

Hopkins, T. S., The GIN Sea: A synthesis of its physical oceanography and literature 1972–1985, *Earth Sci. Rev.*, *30*, 175–318, 1991.

Huntley, D. A., Tides on the north-west European continental shelf, in *The North-West European Shelf Seas, Oceanogr. Ser.*, vol. 24B, edited by F. T. Banner, M. B. Collins, and K. S. Massie, pp. 301–351, Elsevier, New York, 1980.

Huthnance, J. M., Sub-tidal motion on the Scottish continental shelf, August–September 1971, *Cont. Shelf Res.*, *1*, 221–236, 1983.

Huthnance, J. M., Slope currents and "JEBAR," *J. Phys. Oceanogr.*, *14*, 795–810, 1984.

Huthnance, J. M., The Rockall Slope Current and shelf-edge processes, *Proc. R. Soc. Edinburgh, Sect. B, Biol. Sci.*, *88*, 83–101, 1986.

Levitus, S., Climatological atlas of the world ocean. *NOAA Prof. Pap. 13*, 173 pp., U.S. Gov. Print. Off., Washington, D. C., 1982.

Meincke, J., Convection in the oceanic waters west of Britain, *Proc. R. Soc. Edinburgh, Sect. B, Biol. Sci.*, *88*, 127–139, 1986.

Mellor, G. L., An equation of state for numerical models of oceans and estuaries, *J. Atmos. Oceanic Technol.*, *8*, 609–611, 1991.

Mellor, G. L., and T. Yamada, Development of a turbulence closure model for geophysical fluid problems, *Rev. Geophys.*, *20*, 851–875, 1982.

Oey, L.-Y., Simulation of mesoscale variability in the Gulf of Mexico: Sensitivity studies, comparison with observations, and trapped wave propagation, *J. Phys. Oceanogr.*, *26*, 145–175, 1996a.

Oey, L.-Y., Flow around a coastal bend: A model of the Santa Barbara Channel eddy, *J. Geophys. Res.*, *101*, 16,667–16,682, 1996b.

Oey, L.-Y., Eddy energetics in the Faroe-Shetland Channel: A model resolution study, *Cont. Shelf Res.*, in press, 1998.

Oey, L.-Y., and P. Chen, A model simulation of circulation in the northeast Atlantic shelves and seas, *J. Geophys. Res.*, *97*, 20,087–20,115, 1992.

Proctor, R., and A. M. Davies, A three dimensional hydrodynamic model of tides off the north-west coast of Scotland, *J. Mar. Syst.*, *7*, 43–66, 1996.

Samuel, P., J. A. Johannessen, and O. M. Johannessen, A study on the inflow of Atlantic water to the GIN Sea using Geosat altimeter data, in *The Polar Oceans and Their Role in Shaping the Global Environment, Geophys. Monogr. Ser.*, vol. 85, edited by O. M. Johannessen, R. D. Muench, and J. E. Overland, pp. 95–108, AGU, Washington, D. C., 1994.

Saunders, P. M., Cold outflow from the Faroe Bank Channel, *J. Phys. Oceanogr.*, *20*, 29–43, 1990.

Smith, S. D., Wind stress and heat flux over the ocean in gale force winds, *J. Phys. Oceanogr.*, *10*, 709–726, 1980.

Worthington, L. V., The Norwegian Sea as a Mediterranean Basin, *Deep Sea Res. Oceanogr. Abstr.*, *17*, 77–84, 1970.

Xing, J., and A. M. Davies, Application of turbulence energy models to the computation of tidal currents and mixing intensities in shelf edge regions, *J. Phys. Oceanogr.*, *26*, 417–447, 1996a.

Xing, J., and A. M. Davies, Processes influencing the internal tide, its higher harmonics and tidally induced mixing on the Malin-Hebrides Shelf, *Prog. Oceanogr.*, *38*, 155–204, 1996b.

L.-Y. Oey, Atmospheric and Oceanic Sciences Program, Sayre Hall, Forrestal Campus, Princeton University, Princeton, NJ 08544. (e-mail: lyo@splash.princeton.edu)

(Received April 24, 1997; revised December 23, 1997; accepted March 9, 1998.)